Journal of Hazardous Materials 442 (2023) 130032

Contents lists available at ScienceDirect

Journal of Hazardous Materials

journal homepage: www.elsevier.com/locate/jhazmat

V and Cr substitution in dicalcium silicate under oxidizing and reducing conditions – Synthesis, reactivity, and leaching behavior studies

Muhammad Jawad Ahmed [a,*], Remco Cuijpers [a], Katrin Schollbach [a], Sieger Van Der Laan [b], Mary Van Wijngaarden-Kroft [b], Tiny Verhoeven [c], H.J.H. Brouwers [a]

[a] Department of Built Environment, Eindhoven University of Technology, Eindhoven, the Netherlands
[b] Tata Steel, R&D, Microstructure & Surface Characterization (MSC), IJmuiden, the Netherlands
[c] Department of Chemical Engineering and Chemistry, Eindhoven University of Technology, Eindhoven, the Netherlands

HIGHLIGHTS

- Cr and V doped C_2S was synthesized via the sol-gel method.
- Reducing conditions restrict the incorporation of Cr and V in C_2S.
- Stabilization of α´-C_2S can be attributed to matrix constraint.
- Cr and V incorporation reduces reactivity compared to a reference.

GRAPHICAL ABSTRACT

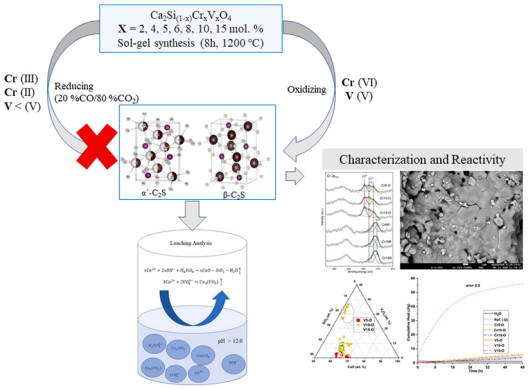

ARTICLE INFO

Editor: <Haizhou Liu>

Keywords:
Sol-gel synthesis
Reducing conditions
Cr and V doped C_2S
Oxidation state
Polymorphs
Leaching

ABSTRACT

Dicalcium silicate (C_2S) is known to incorporate potentially hazardous metals (Cr and V) in a belite-rich cementitious system. The effect of the electrovalence nature of V and Cr on C_2S polymorphs' (α, β, γ) stability under oxidizing and reducing conditions as well as their reactivity are systematically investigated via analyzing oxidation states, phase composition, bonding system, and microstructure as well as oxide composition quantitively. It is shown that C_2S can incorporate Cr (VI) and V(V) consequently leading to stabilization of α, β-C_2S. Instead, Cr (II, III) and V < (V) tend not to substitute in C_2S. Despite reactive polymorphs (α, β-C_2S) stability due to Cr (VI) and V(V) incorporation, the early age (48–72 h) C_2S reactivity is drastically reduced due to Cr (VI) and V (V) incorporation. Moreover, one batch leaching test revealed that the V (V) leaching is inversely proportional to aqueous Ca^{2+} ion at pH > 12 while Cr leaching is sensitive to its oxidation state, and dissolution of C_2S. Even though C_2S can incorporate Cr (VI) and V (V) ions, the final leaching is governed by the immobilization potential of C-S-H gel, pH as well as types of calcium chromate and vanadate complexes.

* Corresponding author.
E-mail address: m.ahmed@tue.nl (M.J. Ahmed).

https://doi.org/10.1016/j.jhazmat.2022.130032
Received 30 May 2022; Received in revised form 13 September 2022; Accepted 17 September 2022
Available online 20 September 2022

1. Introduction

Ordinary Portland cement (OPC) is one of the most used artificial materials in the world. Cement manufacturing requires high energy and resource consumption leading to significant CO_2 footprints (Ludwig and Zhang, 2015; Benhelal et al., 2013). Substantial efforts have been made in developing alternative raw materials and adjusting clinker composition to address the challenges for the sustainable development of the cement industry (Zhu et al., 2021; Lin et al., 1996; Omotoso et al., 1995; Romano and Rodrigues, 2008; Goh and Gan, 1996; Pang et al., 2022; Cuesta et al., 2021). Industrial by-products such as iron and steel making slag, electroplating sludge, and metal surface galvanic sludge are being investigated as alternative raw materials for clinker production (Pérez-Villarejo et al., 2015; Silva et al., 2007). However, these materials contain potentially toxic elements (PTEs) e.g., Cr, V, Ni, As, and their content is strictly regulated by European environmental legislation (Kaja et al., 2021). Therefore, the leaching of PTEs hinders the potential use of these materials for a sustainable future (Spooren et al., 2016; Alam et al., 2019).

Dicalcium silicate (C_2S) is a major constituent of basic oxygen furnace (BOF) slag, belite-based clinker, and a minor constituent of OPC (Aranda, 2016; van Zomeren et al., 2011). Cr and V are among the most abundant heavy metals within the BOF slag (Chaurand et al., 2007). The presence of V and Cr in BOF steel slag, its toxicity, and the potential mobility in leachate have attained significant attention due to environmental implications. V and Cr can get incorporated into the C_2S and therefore their mobility, as well as toxicity, depends on the chemical nature of the host matrix (redox potential, solubility, reactivity, etc.), oxidation state, and substitutable vacancy in the crystal lattice (Ca or Si-site) (Guo et al., 2016). The aliovalent nature of Cr and V, and their tendency to occupy the Ca or Si site in C_2S dictates the enrichment mechanism in the host matrix and leaching behavior (Neuhold et al., 2019; Stewart et al., 2018; Wu et al., 2011). Therefore, a good knowledge of V and Cr substitution in C_2S under varying sintering (oxidizing and reducing) conditions is required for understanding their chemical and environmental impact.

C_2S exists in several polymorphs such as x, α, α'_L, α'_H, β, and γ (Wesselsky and Jensen, 2009). The stable γ-polymorph at room temperature is well known for the lower reactivity as compared to other C_2S polymorphs (x, α, α'_L, α'_H, β) (Lin et al., 1996; Omotoso et al., 1995; Romano and Rodrigues, 2008; Thomas et al., 2017; Zhu et al., 2021). The incorporation of Cr and V chemically stabilizes α' or β-C_2S which can affect its reactivity (Li et al., 2019). The substitution of an ion on Ca or Si-site in C_2S can be predicted using the structure difference factor (D) which is based on the radius, electrovalence, and electronegativity of the substituent (Wensheng et al., 2022). The D factor indicates that the heavy metal ions having an oxidation state > (II) mostly occupy the Si-site in C_2S (Ludwig and Zhang, 2015). The incorporation and replacement of SiO_4^{4-} in C_2S by smaller ions of higher negative valency (e.g., BO_4^{5-}) is effective in the stabilization of β-C_2S (Lopatin and Chizhikova, 2007). If an RO_4 ion is substitutionally accepted in the C_2S lattice on SiO_4^{4-}, a further reorganization requires to preserve the charge neutrality of the total system (Black et al., 2003a; Lai et al., 1992; Maycock and McCarty, 1973). The substitution of anionic position (SiO_4^{4-}) is difficult to study in stochiometric mixes. Alternatively, the substitution of Cr and V in C_2S can be observed by creating a vacancy on the Si-site when reactants are in a non-stochiometric ratio (Wu et al., 2013). It has also been recognized that the oxidation state of Cr and V is controlled by the oxygen (pO_2) partial pressure or sintering atmosphere. The use of reducing sintering conditions is one of the methods to prevent the formation of a high oxidation state of Cr (VI) and V(V) (Trezza and Scian, 2007; Chen et al., 2013).

A few studies have been conducted to investigate the doping behavior of V and Cr in C_2S (Lin et al., 1996; Suzuki et al., 2016; Fierens and Tirlocq, 1983; Parkash et al., 2015a). But there is not much information available for V substitution on Si-site in C_2S. For example, at which oxidation state Cr and V prefer to substitute on the Si-site in C_2S is an important question. This also holds for the maximum amount of substitution of Cr and V on the Si-site in C_2S under certain oxidizing and reducing conditions. In this regard, the systematic understanding of the Cr and V occupation on the Si-site in C_2S under well-defined calcination (oxidizing and reducing) conditions, the oxidation state, impact on reactivity, and environmental impact is necessary for the valorization. Such analytical studies would help to understand the aliovalent Cr, V distribution in C_2S, and its correlation with leaching behavior in Cr, V bearing C_2S phases in belite-based binders, slags as well as sludges.

This study investigates the oxidation state of V and Cr substituted on Si-site in C_2S quantitively under oxidizing (air) and reducing (20 %CO/80 %CO_2) sintering conditions. The effect of Cr and V doping on C_2S polymorphs is correlated with their oxidation states quantitively by using XPS (X-ray photoelectron spectroscopy), QXRD (Quantitative X-ray diffraction), FTIR (Fourier transform Infrared spectroscopy), and SEM-EDX (scanning electron microscopy-energy dispersive X-ray analysis). Furthermore, the early-stage hydration is studied via isothermal calorimetry and thermal gravimetric analysis (TGA) to understand the effect of Cr and V substitution on C_2S reactivity by considering the important factors such as lime, water to solid ratio (w/s), type of C_2S polymorphs, and specific surface area (SSA). Lastly, the Cr and V mobility in aqueous solution is correlated with substitution on Si-site in C_2S, oxidation state, the extent of the C_2S dissolution as well as phase composition by using ICP-OES (inductively coupled plasma-optical emissions spectroscopy) and IC (ion chromatography).

2. Material and methods

$Ca(NO_3)_20.4H_2O$ (Sigma-Aldrich CAS: 13477–34–4, ≥99.0 %), Cr(III)$(NO_3)_30.9H_2O$ (Sigma-Aldrich CAS: 7789–02–8, 99.0 %), V(IV)O$(C_5H_7O_2)_2$ (Sigma-Aldrich CAS:3153–62–2, ≥98.0 %), $Si(OC_2H_5)_4$ (Sigma-Aldrich CAS:78–10–4, ≥99.0 %), HNO_3 (Sigma-Aldrich, CAS:7697–37–2, ≥65 %) and C_2H_5OH (Sigma-Aldrich CAS:64–17–5) were used as received. The reagents were added in the stoichiometric ratios corresponding to the synthesis of C_2S (dicalcium silicate) unless indicated otherwise.

The chemical composition, sample labeling, calcination temperature, and time are summarized in Table 1. To avoid confusion between the Oxygen "O" symbol and sample labeling, the "O" is hyphenated (-O) in this whole manuscript.

2.1. Non-aqueous sol-gel synthesis

The TEOS (tetraethyl orthosilicate) and $Ca(NO_3)_20.4\ H_2O$ (calcium nitrate tetrahydrate) were employed as a source of Si and Ca at molar ratio. TEOS was mixed with ethanol at a molar ratio of 1:5 separately. After this the $Ca(NO_3)_20.4H_2O$, Cr(III)$(NO_3)_30.9H_2O$, and V(IV)O$(C_5H_7O_2)_2$ were dissolved in a minimum amount of ethanol. Then both solutions were mixed followed by the dropwise addition of HNO_3 to reach a pH between 2 and 3. The samples were left overnight, and a translucent gel was obtained. The gel was dried at 150 °C to obtain the

Table 1
Sol-gel synthetic parameters as calcined at 1200 ℃ for 8 h under oxidizing and reducing conditions.

Chemical Composition of the System	Calcination condition	Short description
Ca_2SiO_4	Oxidizing	Ref. (-O)
Ca_2SiO_4	Reducing	Ref. (R)
$Ca_2Si_{(1-x)}Cr_xO_4$ (X = 5, 10, 15)	Oxidizing	Cr(5, 10, 15)-O
$Ca_2Si_{(1-x)}V_xO_4$ (X = 5, 10, 15)	Oxidizing	V(5, 10, 15)-O
$Ca_2Si_{(1-x)}Cr_xO_4$ (X = 2, 4, 6, 8, 10, 15)	Reducing (20 %CO/80 % CO_2)	Cr(2, 4, 6, 8, 10, 15)R
$Ca_2Si_{(1-x)}V_xO_4$ (X = 2, 4, 6, 8, 10, 15)	Reducing (20 %CO/80 % CO_2)	V(2, 4, 6, 8, 10, 15) R

intermediate product, which was then ground, pressed into a pellet, place in the oven at room temperature, and calcined at 1200 °C for 8 h using a heating rate of 5 ℃/min. For oxidizing conditions, the sample is heated in a Nabertherm high-temperature furnace HTCT (LC011H6SN) under a standard air atmosphere. After heating the sample to the desired temperature, it is cooled naturally in the furnace. The rate of furnace cooling is adapted from the oxidizing furnace as shown in Fig. 1(b) and is also used for synthesis under reducing conditions to rule out the different cooling rate effects on the end product (Jawad Ahmed et al., 2022).

For the reducing condition calcination, the furnace was heated to 1200 °C in the heated zone. The dried intermediate gel was weighed and placed on a ceramic (Corundum) disk in the cold part, on the bottom, of the furnace, as shown in Fig. 1(a). The sample was first heated to 700 °C at 5 °C/min. under the oxidizing condition to complete the hydrolysis of $Si(OC_2H_5)_4$ through condensation reaction and remove all the carbon (see Supplementary information S1-thermal gravimetric analysis). The furnace was flushed with Argon gas with a high flow rate to remove the oxygen. After the gas flow was changed to a reducing gas mixture (2 l/min. 20 % CO/80 % CO_2). The sample was then lowered into the heated zone, with a speed that corresponds to a heating rate of 5 °C/min. The sample stayed at 1200 °C for 8 h. The furnace was again flushed with Argon gas before the removal of the sample. The rate of furnace cooling for oxidizing and reducing conditions is shown in Fig. 1(b).

2.2. Characterization techniques

X-ray powder diffractograms were acquired using a Bruker D2 and D8 diffractometer with an X-ray source (Co Kα1 1.7901 Å). A linear position-sensitive detector (LynxEye) was used in 1D mode and a PSD opening of 4°. The instrument had a fixed divergence slit with an opening of 0.5° and 0.04 rad Soller slits. Reflections were measured between 5° and 90° 2 Theta with a step size of 0.02°. Each increment was measured for 2 s. All samples for qualitative and quantitative analysis were prepared via back-loading. The synthesized phases were identified with X'Pert Highscore Plus 2.2 employing the ICDD PDF-2 database.

For Rietveld quantitative phase analysis (RQPA) 10 wt% silicon was added to the samples. Quantitative XRD samples were homogeneously mixed utilizing a McCrone micronizing mill (Retsch). Quantification was done with TOPAS 4.2 software from Bruker. All crystal structures for quantification were obtained from the ICSD database (Table S2). The error values given in the results are the errors as calculated by TOPAS.

The infrared spectra were measured with a Fourier transform infrared (FT-IR) spectrometer from Perkin Elmer FrontierTM. The spectrometer was equipped with a diffuse reflectance accessory. Sixty scans are acquired with optical retardation of 0.25 cm and a resolution of 4 cm^{-1} from 400 to 4000 cm^{-1}.

Scanning electron microscopy (SEM) and energy-dispersive X-ray spectroscopy (EDX) analysis were performed via dispersing the powder on a carbon sticker followed by coating with Pt-Pd. A JEOL JSM-7001F SEM equipped with two 30 mm^2 SDD detectors (Thermo Fisher Scientific) with an accelerating voltage of 10 kV and a beam current of 1.4 nA was employed.

The XPS measurements are carried out with a Thermo Scientific K-Alpha, equipped with a monochromatic small-spot X-ray source and a 180° double-focusing hemispherical analyzer with a 128-channel detector. Spectra were obtained using an aluminum anode (Al Kα = 1486.6 eV) operating at 72 W and a spot size of 400 μm. Survey scans were measured at constant pass energy of 200 eV and region scans at 50 eV. The background pressure was 2×10^{-9} mbar and during measurement 3×10^{-7} mbar Argon because of the charge compensation dual-beam source. The quantification was performed by using CasaXPS (version 2.3.23rev 1.2k) software.

2.3. Reactivity and leaching analysis

To reduce the influence of the particle size distribution (PSD) on the hydration kinetics, the synthesized powder was sieved to narrow the size distribution to 20–40 μm as shown in Fig. 2(a and b). The PSD was measured using a Mastersizer 2000, with a Hydro 2000S wet dispersion unit. The sample was dispersed in isopropanol. The specific surface area [SSA] was determined via PSD estimation as shown in Table 2.

The reactivity was monitored using a TAM Air isothermal calorimeter at 20 °C. Water to solid (w/s) ratios of 0.5, 1.0, and 1.6 were employed. The samples were mixed with the water by hand for one minute before adding the sealed glass ampoules into the calorimeter.

Thermogravimetric analysis was performed using a Jupiter STA 49 F1 from Netzsch. The sample was heated from 40 ℃ to 1000 °C at the rate of 15 K/min under an N_2 or air atmosphere.

For the batch leaching test, C_2S and deionized water were mixed in a 1:10 ratio in plastic bottles. The mixtures were put on a shaker for 24 h at 21 ± 2 °C according to NEN-EN 12457. The obtained suspension was filtered using 0.2 μm polyethersulfone membrane filters and stored at 5 °C after acidifying with nitric acid (65 %, supra pure) to prevent precipitation. Before acidification, the pH was measured. A Spectroblue FMX36 inductive coupled plasma optical emission spectrometer (ICP-OES) was used for Cr, V, and Si determination. Ion chromatography (IC)

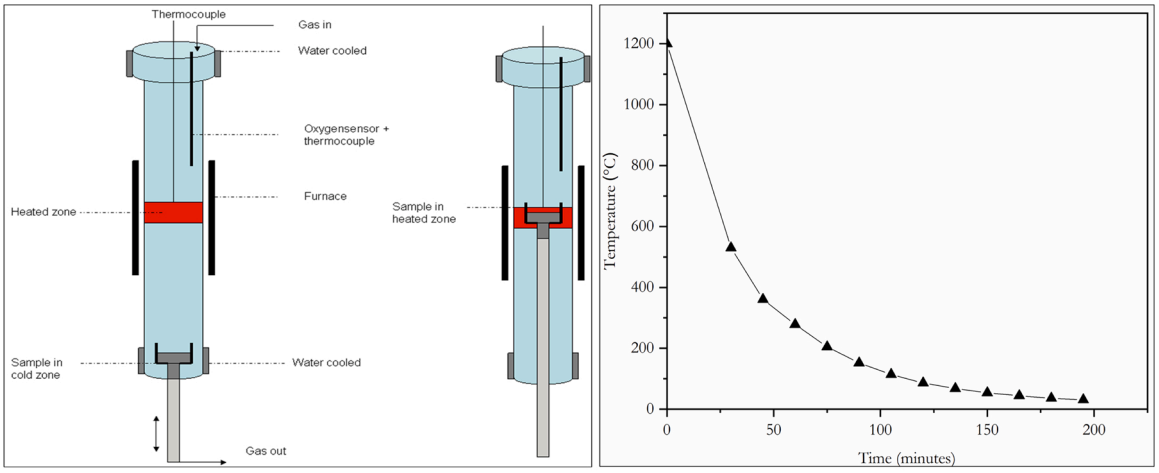

(a) (b)

Fig. 1. The heating furnace (a) the Gero furnace used for calcination under reducing conditions (20 % CO/80 % CO_2) (b) furnace cooling rate.

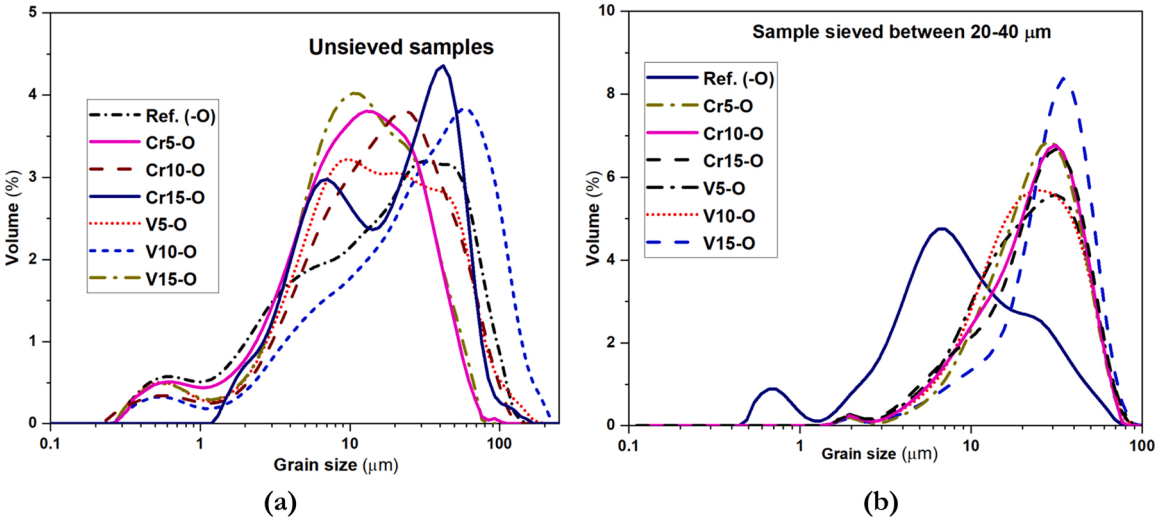

Fig. 2. Cr and V doped C_2S under oxidizing conditions (a) non-sieved sample (b) sample sieved between 20 and 40 μm.

Table 2
The specific surface area (SSA) of the samples.

	unit	Ref. (-O)	Cr5-O	Cr10-O	Cr15-O	V5-O	V10-O	V15-O
SSA (Sieved 20–40 μm)	m^2/g	3.8	2.1	2.1	2.1	1.8	1.8	1.6
SSA (unsieved)	m^2/g	2.9	4.6	4.3	5.3	5.5	4.4	2.9

was used for determining Ca, using a device from Thermo Fisher (Dionex ICS-1100).

3. Result and discussion

3.1. Characterization of the synthesized product

3.1.1. Cr doped C_2S

The QXRD of the Cr doped C_2S under oxidizing and reducing conditions is given in Table 3. The results showed that the replacement of silicon with chromium prevents the formation of γ-C_2S because only the Ref. (-O) contains this polymorph (16.7 wt%) (see Supplementary Fig. S3 (a) for XRD pattern and peak assignment). The Cr5-O sample exhibits a substantial increase in the amount of β-C_2S from 75.1 to 87.8 wt% and stabilization of α′-C_2S (5.3 wt%) as compared to the Ref. (-O) sample. As the replacement level increases from Cr5-O to Cr15-O, the α′-C_2S increases from 5.3 to 43.3 wt% with a decreasing amount of β-C_2S from 87.8 to 24.5 wt% which indicates the incorporation of Cr in C_2S. The stabilization of high-temperature polymorph α′-C_2S at room temperature is usually associated with the exsolution of impurity ions such as Na_2O, K_2O, etc (Lai et al., 1992) and Cr_2O_3 could contribute in the same manner. The impurity ion hinders the transformation of α′ to γ-C_2S during the cooling process. Consequently, the metastable α′-C_2S persists around 675–750 °C, and upon further cooling, to room temperature, it partially collapses to β-C_2S (Elhoweris et al., 2020a). In addition to high-temperature polymorphs (α′ and β) of C_2S, other chromium-bearing

Table 3
QXRD of the chromium-doped C_2S synthesized via the sol-gel process under oxidizing and reducing (20 % CO/80 % CO_2) conditions at 1200 ℃ for 8 h.

Phases (wt%)	Ref. (-O)	Cr5-O	Cr10-O	Cr15-O	Ref. (R)	Cr2R	Cr4R	Cr6R	Cr8R	Cr10R	Cr15R
α′-C_2S		5.3 ± 0.2	23.1 ± 0.3	43.3 ± 0.6							
β-C_2S	75.1 ± 0.3	87.8 ± 0.3	46.9 ± 0.4	24.5 ± 0.6	70.4 ± 0.8	61.2 ± 0.3	64.1 ± 0.3	61.9 ± 0.2	71.02 ± 0.3	59.2 ± 0.2	58.3 ± 0.3
γ-C_2S	16.7 ± 0.2				1.4 ± 0.3						
Lime	2.7 ± 0.1	1.2 ± 0.06	0.7 ± 0.08	0.6 ± 0.1	7.2 ± 0.2	7.5 ± 0.1	5.6 ± 0.1	7.9 ± 0.1	10.2 ± 0.1	6.7 ± 0.1	10.1 ± 0.1
Calcite		0.7 ± 0.1	0.8 ± 0.1	1.5 ± 0.2	0.4 ± 0.1	1.0 ± 0.1	1.1 ± 0.1	1.1 ± 0.1	1.3 ± 0.1	1 ± 0.1	1.6 ± 0.2
(Para)Wollastonite	0.2 ± 0.1				1.2 ± 0.3	8.7 ± 0.2	13.4 ± 0.0.2	8.2 ± 0.2	9.0 ± 0.2	11.2 ± 0.1	5.6 ± 0.4
Cr_2O_3		0.3 ± 0.06	0.7 ± 0.1	1.3 ± 0.2							
$CaCr_2(III)O_4$						0.6 ± 0.1	0.6 ± 0.1	1.2 ± 0.1	1.6 ± 0.1	1.7 ± 0.1	1.8 ± 0.1
$CaCrSi_4O_{10}$			0.7 ± 0.2								
$Ca_5Cr_{1.82}Si_{1.176}O_{12}$				2.3 ± 0.4							
Quartz+Cristobalite	1.0 ± 0.07	1.1 ± 0.08	0.7 ± 0.1	0.8 ± 0.1	1.7 ± 0.5	0.9 ± 0.07	1.2 ± 0.08	0.9 ± 0.1	1 ± 0.04	1 ± 0.06	0.8 ± 0.08
Grossular	0.6 ± 0.2	0.1 ± 0.09			0.8 ± 0.2						
XRD amorphous	3.8 ± 1.6	3.5 ± 1.5	26.4 ± 1.2	25.8 ± 2.1	17.0 ± 3.5	20.2 ± 0.8	14.1 ± 1.0	19 ± 0.7	6.0 ± 1.1	19.3 ± 0.8	21.7 ± 1.0

phases formed such as Cr_2O_3, the chromium analog to silicocarnotite ($Ca_5Cr_{3-x}Si_xO_{12}$) (Adendorff et al., 1992) as well as minor phases such as lime, calcite, cristobalite, and quartz. Moreover, the amorphous content increases from 2.5 to 26.4 wt% with an increasing amount of Cr replacing Si in samples. To understand the maximum Cr-substitution on the Si-site, a theoretical Cr distribution between C_2S + amorphous content and the rest of Cr-bearing phases such as Cr_2O_3, chromium analog to silicocarnotite, etc. was calculated as shown in Table 4. The distribution of Cr has been calculated by considering the starting stoichiometric oxide composition and the QXRD of the samples. The amount of Cr in Cr-bearing crystalline phases is calculated. For the chromium analog of silicocarnotite, the composition ($Ca_5Cr_{1.82}Si_{1.176}O_{12}$) was assumed based on XRD phase information. If this amount of Cr is subtracted from the total amount of Cr in the system. It follows that the remaining amount is incorporated into the C_2S and amorphous content or both. Although it is not possible to differentiate if the Cr is evenly distributed between C_2S polymorphs and amorphous content. As the amount of total Cr increases from 3.3 to 5 wt% (Cr10-O and Cr15-O respectively), a marginal addition from 2.5 to 2.6 wt% is calculated for C_2S+amorphous phase. Therefore, 2.6 wt% seems to be the maximum that can be incorporated into C_2S+amorphous phase. For amounts higher than 2.6 wt% Cr would crystallize out as separate Cr phases such as Cr_2O_3 or Cr analog of silicocarnotite. The comparison between the Cr concentration in C_2S+amorphous content and QXRD analysis of Cr5-O sample indicates that approximately a maximum of 1.4 wt% (4.1 mol%) Cr can be substituted in C_2S theoretically (Tables 3 and 4). The Cr5-O contains an amorphous content as low as 3.5 ± 1.5 wt % which indicates the Cr is mostly incorporated into α′ and β-C_2S.

Under the reducing (20 %CO/80 %CO_2) condition (Table 3), the reference sample (Ref. (R) exhibits a lower total amount of β/γ-C_2S (70.4 and 1.4 wt%) with higher amorphous content (17.0 wt%) than the Ref. (-O) sample calcined under oxidizing conditions. The presence of high free lime (7.2 wt%) along with wollastonite (1.2 wt%) and quartz + cristobalite (1.7 wt%) indicates the incomplete reaction with the precursors. It would originate due to a little hindrance in sintering reaction between incomplete Si-O-Si network, wollastonite, and calcium oxide due to reducing condition. The complete conversion of reactant into C_2S in sol-gel synthesis partially requires a sintering reaction between the CaO and Si-O-Si network at high temperatures under oxidizing conditions (Jawad Ahmed et al., 2022). As the Si was replaced with 2, 4, 6, 8, 10, 15 mol% Cr under reducing conditions, the β-C_2S (ranging from 58.3 to 71.0 wt%) was the only C_2S polymorph that formed during cooling. Moreover, a considerable amount of lime (5.6–10.2 wt%), (Para)wollastonite (5.6–13.4 wt%) is observed alongside $CaCr_2(III)O_4$ (0.6–1.8 wt%) and high amorphous (6.0–21.7 wt%) content. The high amount of unreacted lime and wollastonite phases point to an imbalanced Ca and Si stoichiometry with a lack of Si content for C_2S synthesis. The stabilization of only β-C_2S, the imbalanced stoichiometry, and high amorphous content under reducing conditions indicate that no Cr was incorporated into C_2S. This could happen due to a change in the Cr oxidation state in reducing conditions as the addition of Cr on Si-site in C_2S is highly dependent on the oxidation state and geometry of the Cr ion (Fierens and Tirlocq, 1983).

FTIR has been chosen to investigate bond systems as shown in Fig. 3 (a, b). Usually, the β-C_2S has a characteristic absorption band in the range of 990–998 cm^{-1} and 860 cm^{-1} due to silica stretching. The intensity of this band decreased, and the broadband appeared indicating the presence of α′-C_2S with an increasing amount of Cr dopant in Cr5-O, Cr10-O, and Cr15-O, as shown in Fig. 3, (a). The carbonation of the sample arising from exposure to air can result in the band at 1490 cm^{-1}, caused by the asymmetric stretching of carbonate (CO_3^{2-}) ions. The small sharp peak at 3650 cm^{-1} is depicting the presence of calcium hydroxide originating due to lime reaction with moisture. In reducing conditions, the broadening of the band around 890 cm^{-1} can be attributed to wollastonite as shown in Fig. 3(b) (Meiszterics et al., 2010).

To understand the Cr occupancy on Si-site in C_2S, the oxidation state of Cr ions has been measured quantitatively in the Cr5-O, Cr6R, Cr10-O, Cr10R, Cr15-O, and Cr15R samples due to approximately the same starting Ca/Si molar ratio of the precursors as shown in Fig. 4. The binding energies of Ca 2p ($2p_{3/2}$: ~347 eV) and Si 2p ($2p_{3/2}$: ~101 eV) agrees with previously reported C_2S values (see XPS elemental analysis Supplementary information Table S4 and S5) (Black et al., 2003, 2003a, b). The separation between Si 2p and Ca 2p binding energies ($\delta_{Ca\text{-}Si}$) was calculated as ~245.7 eV which is slightly lower than the 246.07 eV value reported for β-C_2S (please see Table S5) (Black et al., 2003).

Under oxidizing conditions, a Cr $2p_{3/2}$ peak at binding energy ~579.6 eV is assigned as Cr (VI) which indicates the incorporation of Cr in C_2S. The Cr $2p_{3/2}$ peaks at binding energy ~576.6 and 578.1 eV are assigned to Cr (III) which is predominant in the Cr5-O, Cr10-O, and Cr15-O samples. The shift in binding energy from ~576.6–578.1 eV indicates the presence of Cr (III) in two different sites and orientations (Li et al., 2014; Basak et al., 2018). No Cr (IV) was observed. It is worth mentioning here that the Cr was added as Cr (III) for the synthesis of C_2S. The results indicate that as the amount of Cr increases in the samples, a specific amount of Cr (VI) can be incorporated in C_2S on the Si-site which is approximately the same in all the samples as shown in Fig. 4 (c). However, most of the chromium stayed as Cr (III) either in the form of Cr_2O_3 (~576.6 eV) or bound in a different phase as the shift ~578.1 eV indicates in the measurement. This is most likely the amorphous phase that was observed via QXRD. However, the α′-C_2S stabilization due to the increasing amount of Cr in the samples cannot only be associated with Cr incorporation in C_2S as the amount of Cr (VI) is approximately the same in Cr10-O, and Cr15-O samples (Fig. 4(c), Tables 3 and 4). Some other factors are also contributing alongside the Cr (VI) incorporation in C_2S. This observation is compelling for further characterization of material to understand the phenomenon of α′-C_2S stabilization.

Under reducing conditions, the samples only contained Cr (II) and (III) oxidation states as shown in Fig. 3(a, c). The Cr $2p_{3/2}$ binding energy peak at ~575.4 eV is assigned as Cr (II) (Apte et al., 2006). This observation alone explains a large amount of free lime and (Para) wollastonite phases. Cr (II) and (III) exist in octahedral geometry and tend not to substitute the Si-site in C_2S leading to a silica deficit, which creates (Para)/wollastonite and free lime instead (Table 3) (Suzuki et al., 2016).

SEM-BS (backscattered image) images were taken of Cr5-O, Cr10-O, and Cr15-O as shown in Fig. 5(a, b, c) to gain information about the microstructure. Two different kinds of grains were recognized: smooth grains and grains covered with a glassy layer. The Cr doped C_2S exhibited small and large grains with lamellar morphology as previously reported for the incorporation of other ions (Ghose et al., 1983). The Cr5-O sample exhibited smooth grain with conspicuous grain boundaries (Fig. 5(a)). As the amount of Cr increased in Cr10-O, the individual grain surface was covered with a glass layer as well as grain boundary

Table 4
Theoretical composition calculation of vanadium and chromium distributed among different mineral phases synthesized under oxidizing conditions. The theoretical composition is the difference between the starting amount of heavy elements (Cr, V) and the oxides contained in the C_2S+amorphous as well as Cr/V-bearing phases.

Sample	Total substitution (wt %)	Cr or V in C_2S + Amorphous phases (wt%)	Cr or V in Chromium and Vanadium phases (wt%)
Cr5-O	1.7	1.4	0.3
Cr10-O	3.3	2.5	0.8
Cr15-O	5	2.6	2.4
V5-O	1.7	1.3	0.4
V10-O	3.3	2.3	1
V15-O	5	3.1	1.9

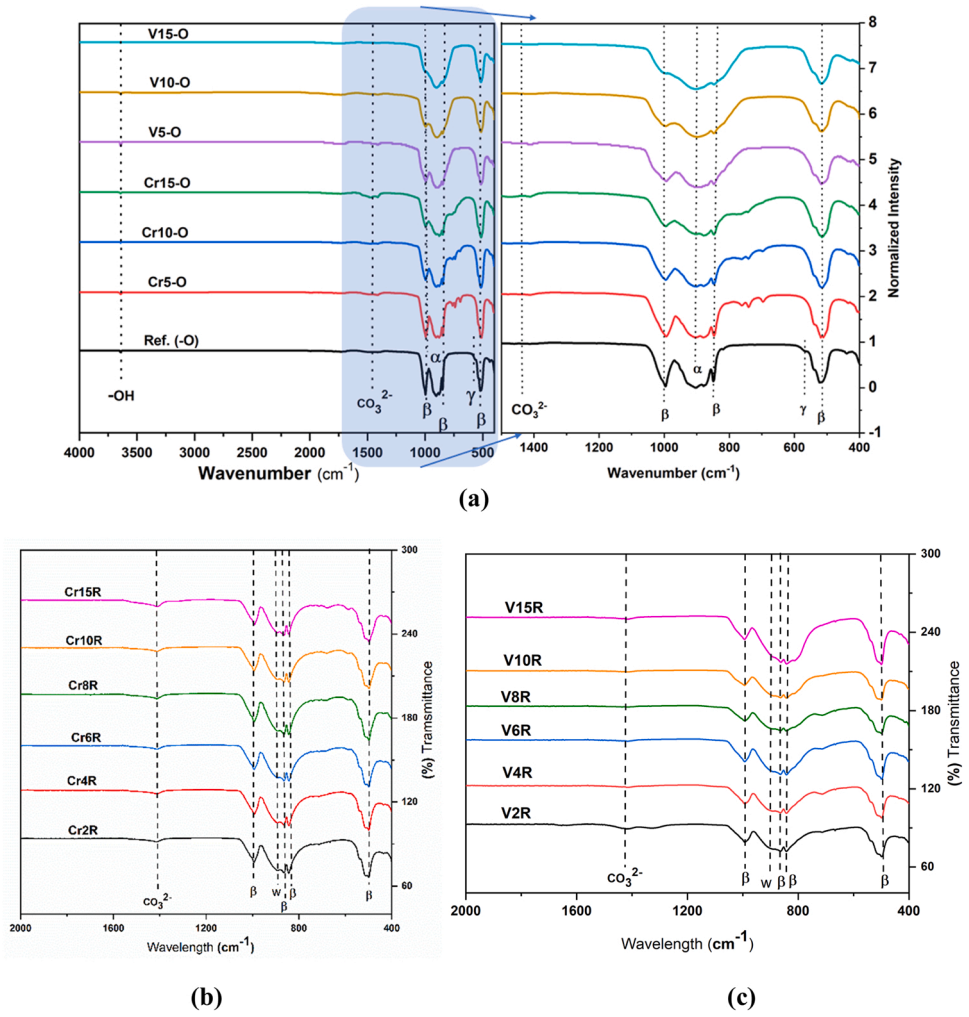

Fig. 3. FTIR analysis Cr and V doped C_2S (a) oxidizing conditions (b) Cr doped C_2S under reducing conditions (c) V doped under reducing conditions.

phase precipitates between the striae (Fig. 5(b)). As the Cr amount further increased in Cr15-O, the individual and multiple grains were covered with a glassy layer observed (Fig. 5(c)) likely due to the formation of the C_2S-Cr_2O_3 glass phase as the Cr amount increases from 5 to 15 mol%. This glassy phase fits with the fact that an increasing amount of amorphous content is detected with the increasing replacement of Si with Cr (Table 3). The stabilization of α′-C_2S in the Cr10-O and Cr15-O samples cannot be attributed to a change in average crystallite size as the small crystallite size favors the formation of α′/β-polymorphs (Fig. S6). Moreover, the α′-C_2S stabilization due to the increasing amount of Cr cannot only be associated with Cr incorporation in C_2S as the amount of Cr (VI) is approximately the same in Cr10-O, and Cr15-O samples (Tables 3, 4, Fig. 4(a)). Persuasively, the average crystallite size is not changing with an increasing amount of Cr. It would rather change due to the matrix constraint (coverage of individual C_2S grain with glass layer) which also contributes toward the α′→β transformation. The free energy of an isolated particle may be considerably different from that of a constrained particle. The glassy layer constraining the C_2S grains restricts the growth of the mean particle size to below a critical size that would cause the transformation from α→β→γ otherwise (Saidani et al., 2018; Chan et al., 1992). Conclusively, the matrix constraint is one of the main reasons behind the stabilization of α′-C_2S with an increasing amount of Cr in the sample.

In addition to SEM BS imaging, EDX spot analysis was performed on the samples to determine the composition. An example of the spots measured is shown in Fig. 6(a, b, c). All measured spots of the synthesized Cr5-O, Cr10-O, and Cr15-O have been plotted in the oxide composition diagram shown in Fig. 6(g). It is worth mentioning here that the resolution is ~1 μm, therefore it is difficult to measure the small features like the glassy layer separately because analysis always includes the underlying phase. However, the amount of Cr increases as the amount of Cr increases in the sample, and the highest amount was observed in the glass layer of the Cr15-O sample. The oxide composition diagram indicated that there is not much difference in the composition of Cr5-O and Cr10-O samples. But in the Cr15-O sample, the distinction between Cr-bearing C_2S phases and Cr-enriched phases became conspicuous in the Cr15-O sample which was also observed in the XRD sample (Table 3).

3.1.2. *V doped C_2S*

The QXRD of V doped C_2S under oxidizing and reducing conditions is shown in Table 5. The replacement of V on the Si-site under oxidizing condition (V5-O) prevents the formation of γ-C_2S (16.7 wt%) that is observed in the reference sample (see Fig. S3 (b) for XRD pattern and peak assignment). Sample V5O exhibited the stabilization of α′-C_2S (8.3 wt%) and β-C_2S (71.8 wt%) alongside minor phases such as free-lime, calcite, quartz, cristobalite, and higher amorphous content (15.4 wt%) than reference sample (3.8 wt%). As the amount of V increased in V10-O, and V15-O samples, more α′-C_2S (27.0 and 27.1 wt% respectively) is stabilized pointing to the incorporation of V on Si-site. The β-C_2S amount decreased from 71.8 to 29.9 wt% with an increasing amount of amorphous content (from 15.4 to 36.2 wt%).

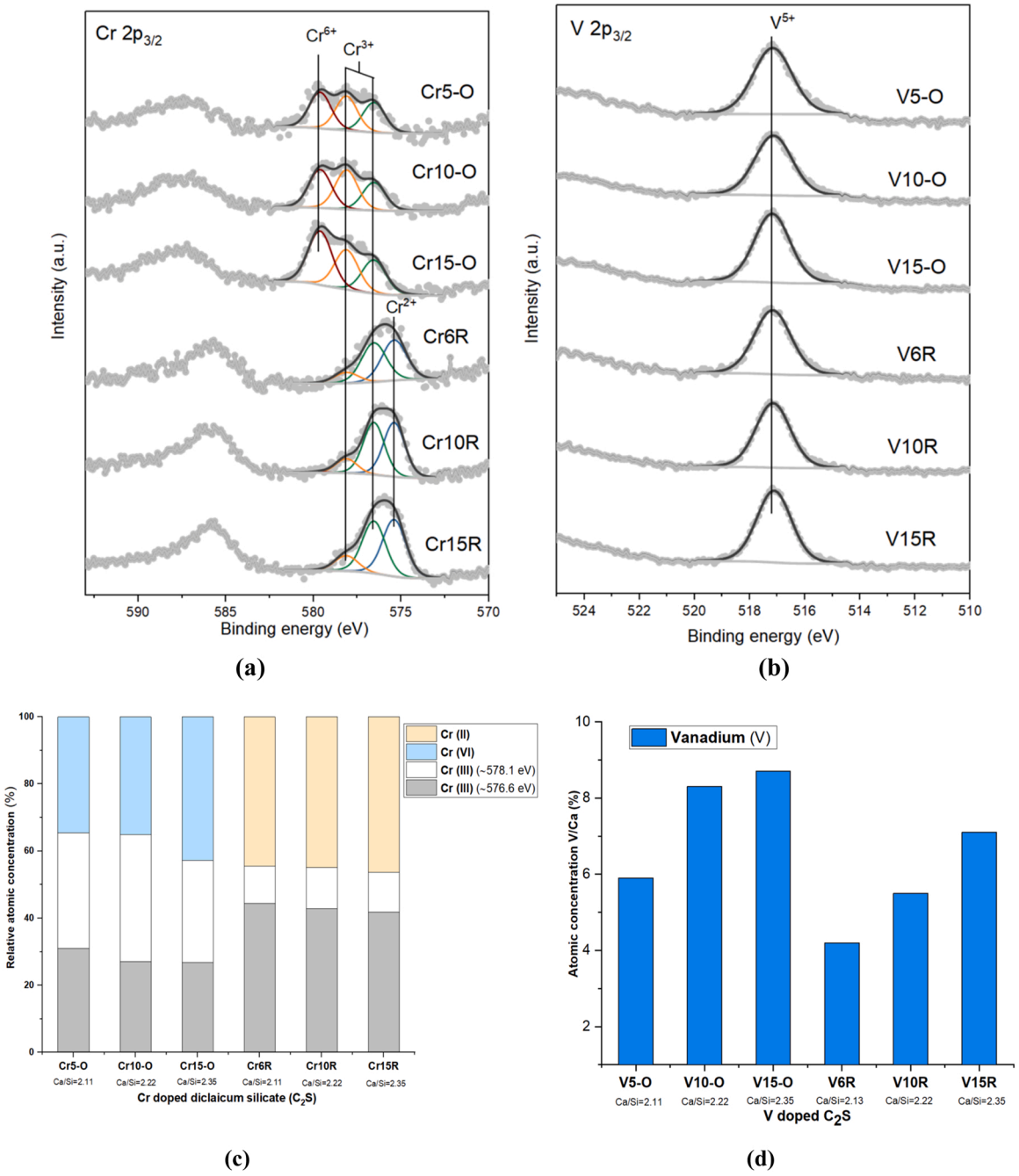

Fig. 4. XPS analysis of Cr and V doped C_2S **(a)** Cr $2p_{3/2}$ scan of Cr doped C_2S **(b)** V $2p_{3/2}$ scan of V doped C_2S **(c)** relative percentage oxidation sate of Cr doped C_2S under oxidizing and reducing condition **(d)** relative Ca/V ratio of V doped C_2S under oxidizing and reducing condition.

Additionally, some vanadium-bearing crystalline minor phases like VO_2 and CaV_2O_4 alongside some calcite, quartz, and cristobalite were observed. The theoretical distribution of V is calculated between C_2S+amorphous phases and V-bearing phases as shown in Table 4. The amount of V increases from 1.3 to 3.1 wt% in C_2S+amorphous phases with an increasing amount of V in the sample. Considering the amount of amorphous content (15.4 ± 1.7 wt%) and vanadium-bearing crystalline phase in V5-O, it is difficult to predict the maximum substitution of V on Si- site in C_2S theoretically.

Under reducing conditions, the V doped C_2S exhibits only β-C_2S polymorph as shown in Table 5. This indicates that vanadium is not incorporated into the C_2S as similar behavior was observed in the case of Cr doping under reducing conditions. The V2R sample contains 72.1 wt % β-C_2S and 9.4 wt% lime as observed in Ref. (R) but a higher amount of (Para)wollastonite (12.4 wt%). As the amount of V replacement increases under reducing conditions (V4R, V6R, V8R, V10R, V15R), the new V-bearing crystalline phases such as V_5O_9, $CaVO_3$, CaV_3O_7, Ca(VO)Si_4O_{10} are observed alongside a high amount of β-C_2S (58.0–67.2 wt%), (Para)wollastonite (6.4–10.3 wt%) and lime (4.2–7.7 wt%). The high amount of (Para)wollastonite and lime indicates that the Ca to Si stoichiometry is imbalanced. Consequently, vanadium is unable to substitute on Si-site in C_2S under reducing conditions due to a geometrical or oxidation state mismatch between the vacancy (Si-site) and the substituent. This leads to the Si deficit and promotes the (Para)wollastonite formation. Such behavior was also observed in Cr under reducing conditions.

XPS analysis was performed to get better insight into the oxidation state of the V5O, V6R, V10O, V10R, V15O, and V15R as shown in Fig. 4.

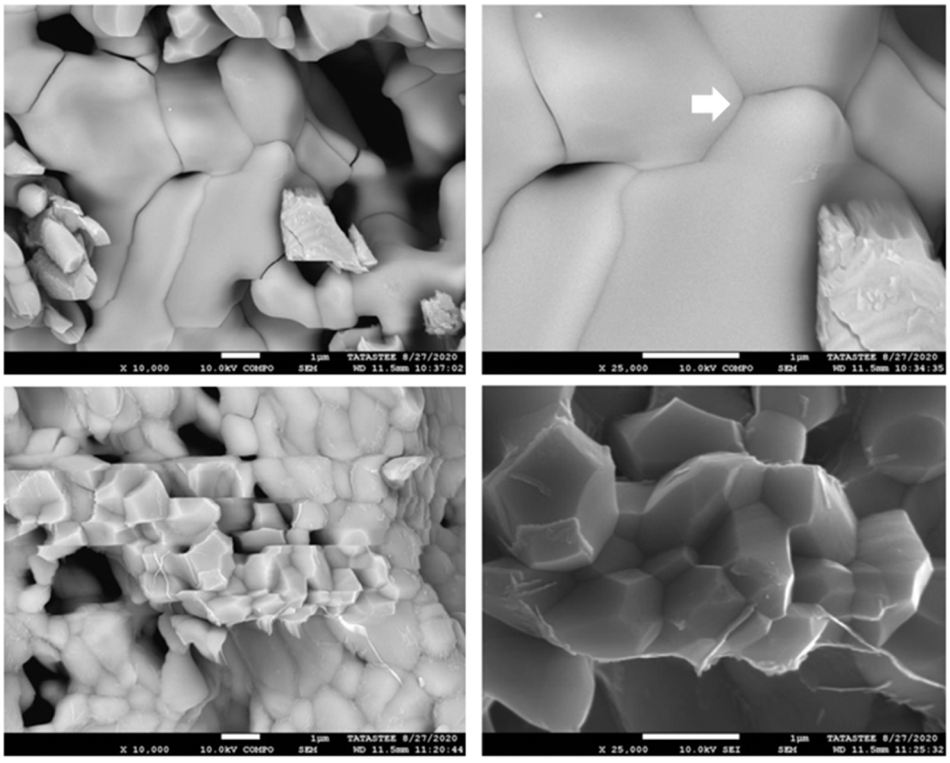

(a)

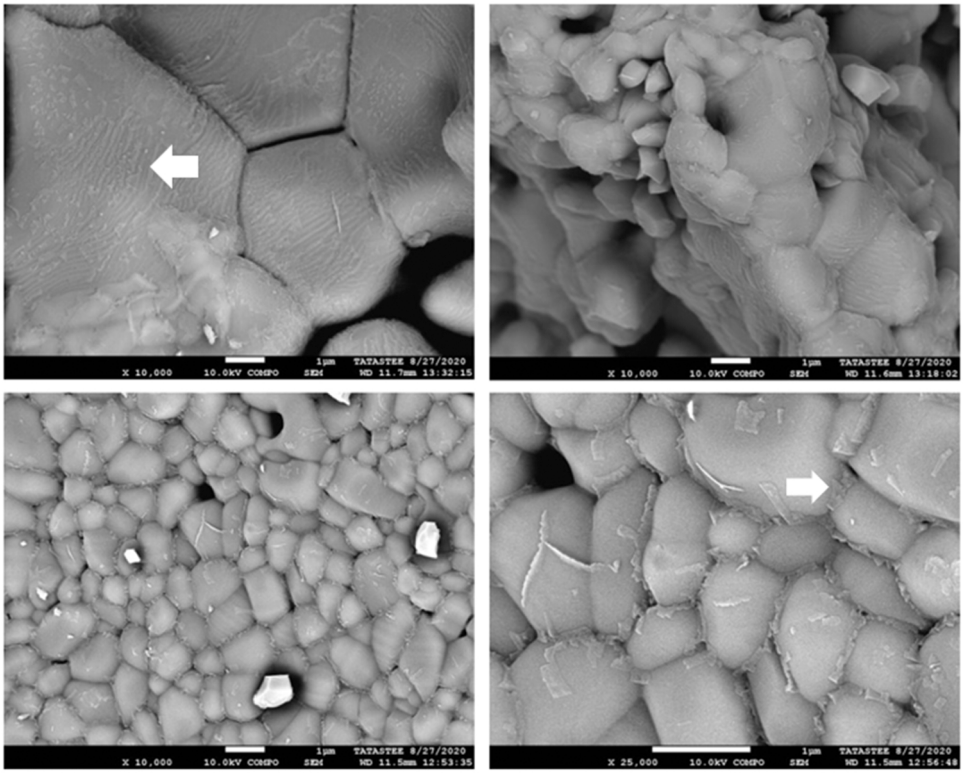

(b)

Fig. 5. SEM (Scanning electron microscopy) analysis of Cr and V doped C_2S under oxidizing conditions (a) Cr5-O (b) Cr10-O (c) Cr15-O (d) V5-O (e) V10-O (f) V15-O. "white arrow" indicates the grain boundaries and "circle" indicates the sign of surface relief.

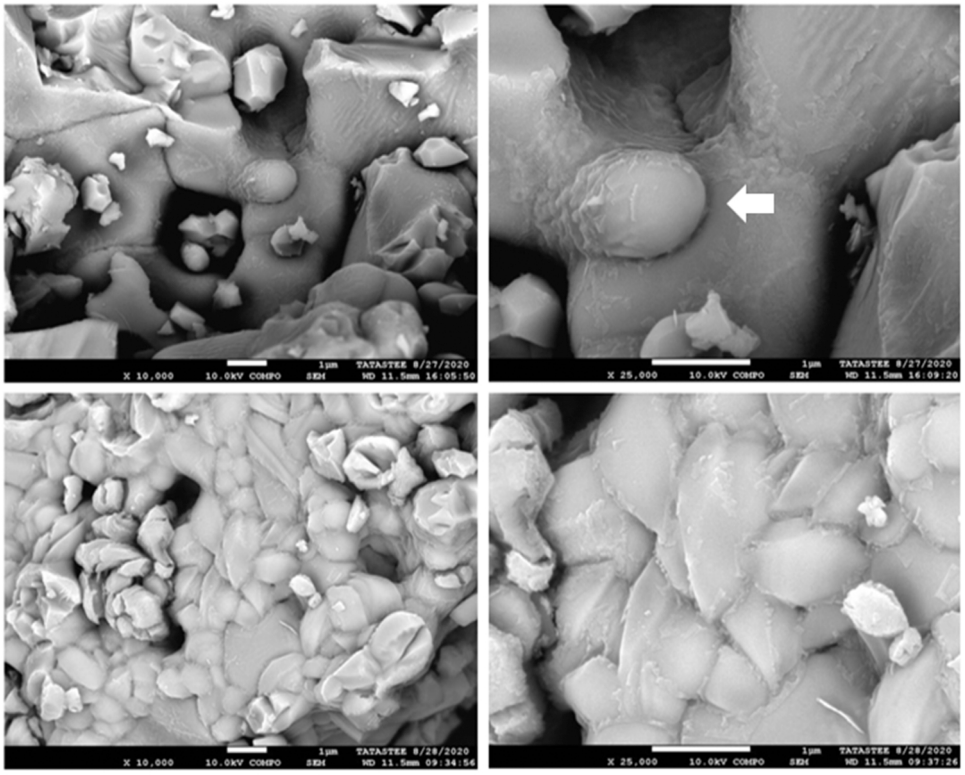

(c)

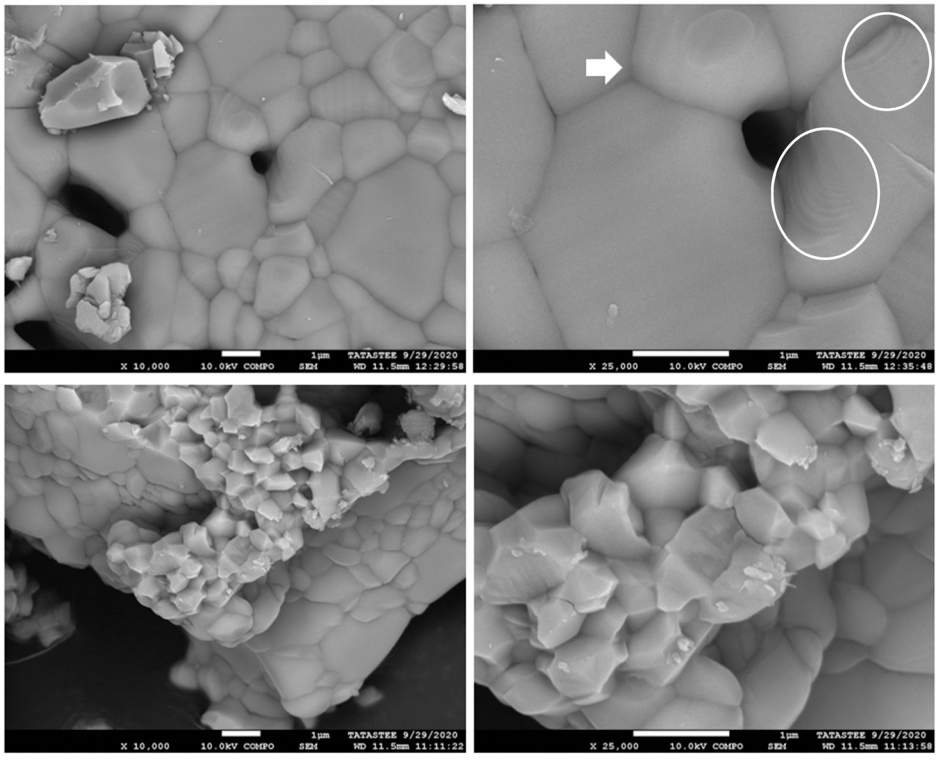

(d)

Fig. 5. (*continued*).

The V $2p_{3/2}$ peak at binding energy ~517.2 eV is assigned as V (V) as shown in Fig. 4(d) (see XPS elemental analysis Supplementary information Table S4) (Silversmit et al., 2004; Lu et al., 1998). The V/Ca atomic concentration (%) is calculated to make a direct comparison between all the measurements as shown in Fig. 3(d). Moreover, Ca is taken as the denominator because the amount of Ca is not changing in all the V doped C_2S samples. Only V (V) found in V5O, V10O, and V15O samples as well as the C_2S samples calcined under reducing conditions

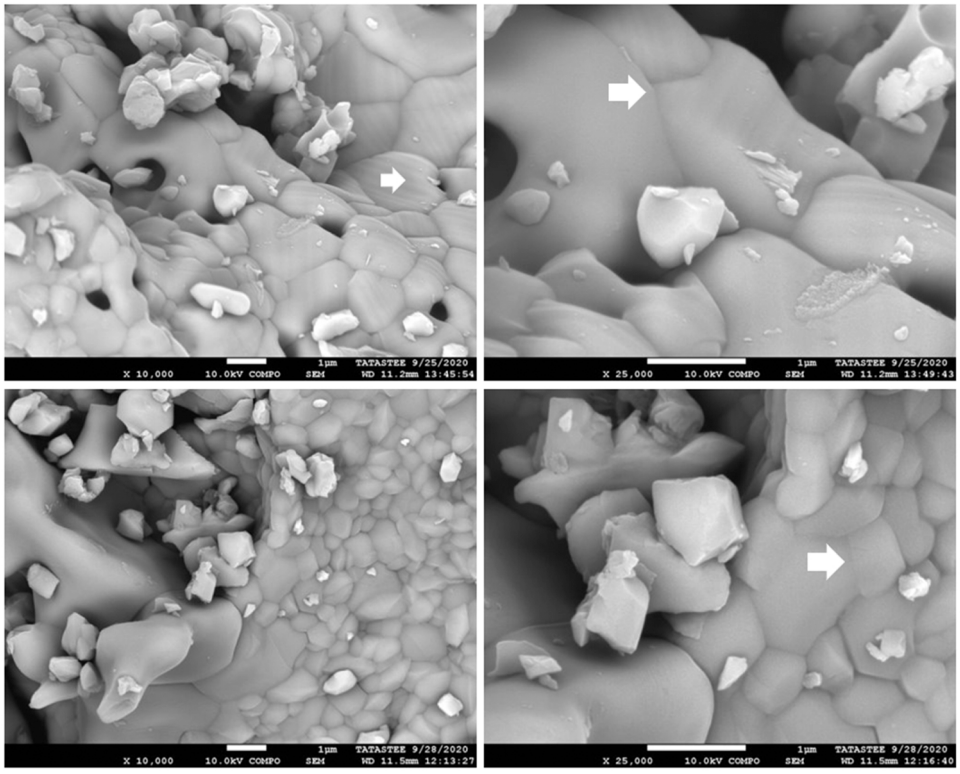

(e)

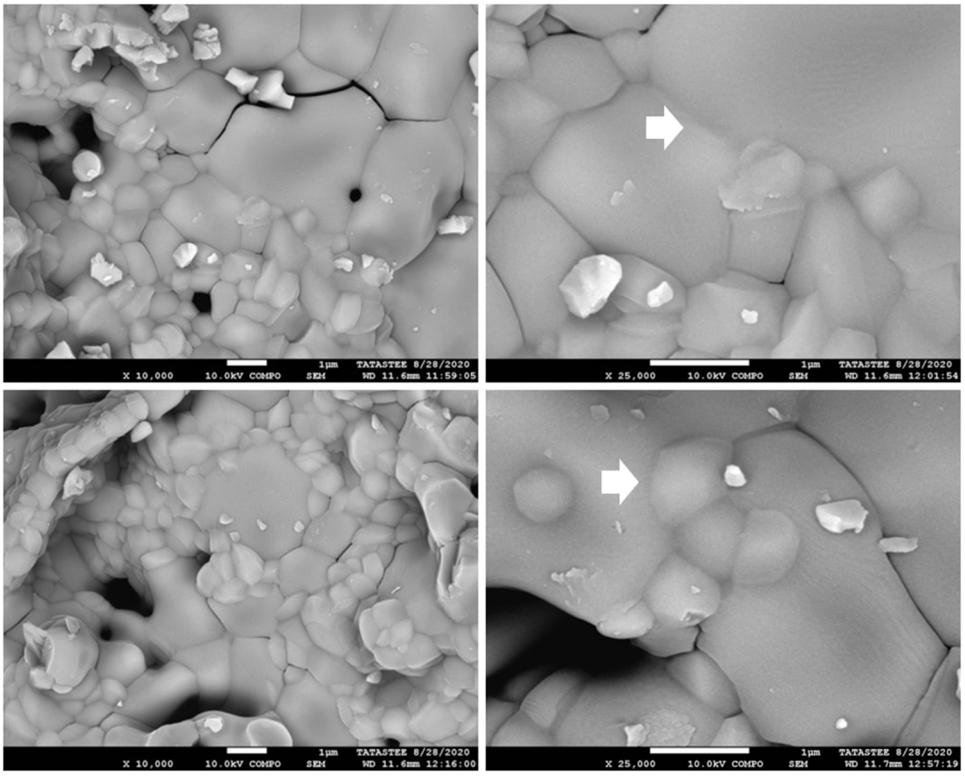

(f)

Fig. 5. (*continued*).

(V6R, V10R, V15R) also exhibit the presence of V (V) in the samples (Fig. 4(b, d). An oxidation state lower than V(V) was not observed. Possibly, the V5R, V10R, and V15R samples fully oxidize to V(V) on cooling because the vanadium (II-IV) oxide is highly sensitive to air oxidation (Lu et al., 1998). The stabilization of α-C_2S with the increasing amount of V indicates the occupation of the Si-site by V(V) due to V_2O_5

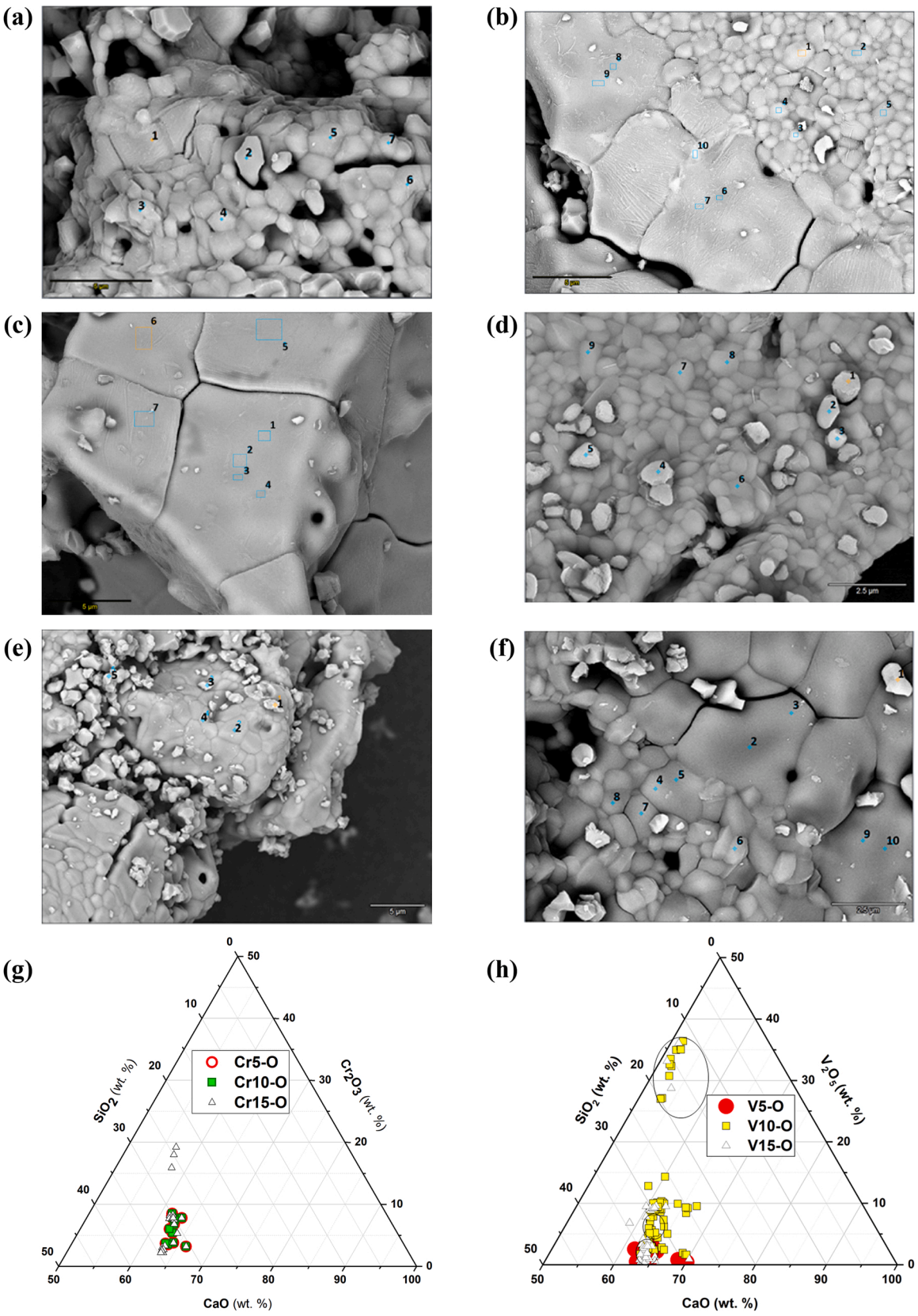

Fig. 6. EDX (Energy dispersive X-ray) analysis of Cr and V doped C_2S under oxidizing conditions-the oxide composition of varying spot positions (a) Cr5-O (b) Cr10-O (c) Cr15-O (d) V5-O (e) V10-O (f) V15-O (g) oxide composition of Cr (5, 10, 15) -O (h) oxide composition of V (5, 10, 15) -O.

Table 5
QXRD of the Vanadium doped C_2S synthesized via the sol-gel process under oxidizing and reducing (20%CO/80%CO_2) conditions at 1200 ℃ for 8 h.

Phases (wt%)	Ref. (-O)	V5-O	V10-O	V15-O	Ref. (R)	V2R	V4R	V6R	V8R	V10R	V15R
α′-C_2S		8.3 ± 0.3	27.0 ± 0.4	27.1 ± 4.8							
β-C_2S	75.1 ± 0.3	71.8 ± 0.5	46.3 ± 0.4	29.9 ± 4.3	70.4 ± 0.8	72.1 ± 0.3	60.3 ± 0.3	60.3 ± 0.3	58.9 ± 0.4	67.2 ± 0.9	58.0 ± 0.5
γ-C_2S	16.7 ± 0.2				1.4 ± 0.3						
Lime	2.7 ± 0.1	2.6 ± 0.08	0.1 ± 0.06	1.6 ± 0.3	7.2 ± 0.2	9.4 ± 0.1	5.0 ± 0.1	5.9 ± 0.1	7.7 ± 0.1	5.5 ± 0.1	4.2 ± 0.1
Calcite		0.3 ± 0.1	1.4 ± 0.2	1.6 ± 0.3	0.4 ± 0.1	0.9 ± 0.1	0.4 ± 0.1	0.7 ± 0.1	0.7 ± 0.2	0.9 ± 0.2	1.7 ± 0.2
Wollastonite+Parawollastonite	0.2 ± 0.1				1.2 ± 0.3	12.4 ± 0.2	10.3 ± 0.2	7.9 ± 0.2	8.8 ± 0.2	6.5 ± 0.3	6.4 ± 0.3
Quartz + Cristobalite	1.0 ± 0.06	1.2 ± 0.1	0.6 ± 0.1	0.6 ± 0.1	1.7 ± 0.5	1.5 ± 0.1	1.3 ± 0.1	1.0 ± 0.1	0.8 ± 0.1	0.8 ± 0.03	1.5 ± 0.1
VO_2		0.4 ± 0.08	0.9 ± 0.2	1.0 ± 0.2		0.3 ± 0.1	0.1 ± 0.1		0.1 ± 0.1		
V_5O_9			0.1 ± 0.3					0.7 ± 0.1	0.7 ± 0.2	1.2 ± 1.0	1.8 ± 0.2
CaV_2O_4				0.9 ± 0.3							
$CaVO_3$								0.5 ± 0.2	0.6 ± 0.2	0.3 ± 0.3	0.4 ± 0.3
CaV_3O_7								0.8 ± 0.1	0.7 ± 0.2	0.8 ± 0.2	1.2 ± 0.2
$Ca(VO)Si_4O_{10}$											0.3 ± 0.1
Grossular	0.6 ± 0.2	0.2 ± 0.1	1.5 ± 0.2	0.8 ± 0.4	0.8 ± 0.2					0.3 ± 0.2	
XRD amorphous	3.8 ± 1.6	15.4 ± 1.7	22.2 ± 1.9	35.2 ± 8.3	17.0 ± 3.5	2.9 ± 1.1	22.5 ± 0.9	21.9 ± 1.0	21.2 ± 1.2	16.7 ± 1.7	24.5 ± 1.2

substituting as the foreign ion (Table 5). Usually, the impurity ions such as V(V) in the present case can only be incorporated as foreign ions at high clinkering temperatures (Elhoweris et al., 2020b). The absence of α′-C_2S and the presence of a high amount of (Para)wollastonite in V6R, V10R, and V15R indicates that the V was not available as V(V) at high temperatures under reducing conditions. Therefore, it was not substituted on Si-site in C_2S.

The presence of vanadium species also complicates the assignment of peaks in FTIR. A representative FTIR spectrum has been chosen to investigate bond systems as shown in Fig. 3(a, c). Usually, the β-C_2S has a characteristic absorption band in the range of 990–998 cm^{-1} and 860 cm^{-1} due to SiO_2- stretching. However, the characteristic V-O-V asymmetric stretch vibrations, as well as V-O-V octahedral bending, lie in the region of 1010–1040 and 840–860 cm^{-1} (Kumar et al., 2021; Frederickson and Hausen, 2002). These two bands′ shoulders are superimposed on a broad peak around 900 cm^{-1} in the stretching region. The α′-C_2S also has a strong and broad characteristic absorption at 895 cm^{-1}. This causes peak broadening in the samples with a higher concentration of α′-C_2S as the amount of the dopant increases in the V5-O, V10-O, and V15-O as shown in Fig. 4(a). Moreover, the broadening of the shoulder around 990–1035 cm^{-1} can be attributed to V═O isolated double bonds (El-Moneim et al., 2022). The α'- and β- C_2S polymorphs both showed a strong absorption around 520 cm^{-1} with a faint shoulder at 540 cm^{-1} in the SiO_2-bending region. In the mixture in which both phases are present, the polymorph-specific absorptions are indistinguishable. The slight carbonation of the sample arising from exposure to air can result in the band at 1490 cm^{-1}, caused by the asymmetric stretching of carbonate (CO_3^{2-}) ions. The small sharp peak at 3650 cm^{-1} can point out the presence of free lime in the sample that was slightly hydrated in the air.

The C_2S sample calcined under reducing conditions (V2R, V4R, V6R, V8R, V10R, and V15R) feature β-C_2S as a dominant phase. But the broadening of signal around 840–860, 890, and 990–1040 cm^{-1} can also be attributed to the presence of wollastonite and vanadium bearing phases in the samples. All these findings showed a good agreement with QXRD and previous reports (Miyata et al., 1987).

An extensive SEM-EDX analysis was performed to get an insight into the microstructure and composition of the V doped C_2S under oxidizing conditions. Sample V5-O exhibited the individual twin domains with distinct grain boundaries and lamellae characteristics (Fig. 5(d)) like the Cr-containing samples. Additionally, a sign of surface relief perpendicular to the twin domain can also be observed which is the characteristic deformation occur during the α′→β transition due to doping of foreign ions in C_2S (Saidani et al., 2021). As the amount of V is increasing in V10-O and V15-O, then more covered individual grains as well as coverage of multiple grains by glass layer indicating the presence of V -bearing amorphous phases (Fig. 5(e, f)). Moreover, the distinct grain boundaries also start to disappear indicating the precipitation of the new phases. Therefore, the increase in the amorphous content and V-bearing crystalline phases were observed in V10-O and V15-O samples matching with the QXRD observation (Table 5).

The oxide composition of V5-O, V10-O, and V15-O samples was measured with EDX on random spots including the precipitate at grain boundaries, smooth grain, and grain covered with a glass layer. A few of the spot data from backscattered images are shown as an example in Fig. 6(d, e, f). It was observed that the V5O sample gave a slightly higher average V_2O_5 concentration in the middle of smooth grains. At high Si replacement with V, the V10-O and V15-O samples exhibited a vanadium concentration as high as 36% in the smooth grains while the average was 1–2 % in the single grains covered with a glass layer. Moreover, the V15-O sample showed the highest V_2O_5 concentration ranges from 5 % to 10 % in the grains covered with a glass layer. All these data points are not coverable in Fig. 6(d, e, f) and therefore, are plotted in the form of an oxide composition diagram as shown in Fig. 6 (h). One of the reasons that the higher concentration of vanadium in the grains up to 36 % than a stoichiometric oxide composition of the mineral phases in the V5-O, V10-O, and V15-O samples would possibly be observed due to the relatively small average crystallite size of α′ and β-C_2S which leads to an overestimation of the vanadium concentration (Table 5) (see average crystallite size in Fig. S6). That's why the oxide composition diagram exhibits some outliers which leads to the wide range of the composition.

The replacement of Si with V in the C_2S matrix leads to the formation of three types of phase composition such as primary C_2S phases, V-rich C_2S phases, and high V-bearing phases as encircled in Fig. 6(h). In the V10-O and V15-O samples, the vanadium started to enrich in separate phases which would be the reason for the high amorphous content (Table 5).

3.2. Hydration studies of Cr and V doped C_2S

Cr and V doped C_2S under oxidizing conditions (Cr5-O, Cr10-O, Cr15-O, V5-O, V10-O, V15-O) were measured via isothermal calorimetry to determine the hydration rate. The heat flow curves normalized to the mass of the solid are presented in Fig. 7. The C_2S reactivity is highly sensitive to the specific surface area, lime (CaO) content, water to solid ratio (w/s), and the type of C_2S (α′, β, γ) polymorph (Thomas et al., 2017; Georgescu et al., 2000). Therefore, the samples were sieved to between 20 and 40 μm, and different w/s ratios were investigated. Usually, the increase in the w/s ratio enhances the degree of dissolution of C_2S (Nicoleau et al., 2013). However, Ref. (-O) sample does not show any significant increase or decrease in the heat release with varying w/s ratio. Instead, a constant cumulative heat ~56 J/g_{C2S} in Ref. (-O) sample is observed with increasing w/s from 0.5 to 1.0 as shown in Fig. 7(b, f). All Cr and V-containing samples show almost no heat release in the first 48 h, except for an initial strong heat flow for the first twenty minutes observed that could be attributed to the dissolution of C_2S phases (El-Didamony et al., 1996). A similar pattern of early heat release was observed in all the samples with varying water to solid ratios (inset of Fig. 7 ((a), (c), (e)). To identify the possible baseline disturbance in the first 20–30 min due to the opening of the calorimeter ampoule, a balanced amount of water was added alongside all the samples and was labeled as H_2O. This way it can be ensured that the exothermic peaks during the first 20–30 min of hydration are indeed coming from the sample as shown in Fig. 7(a, b). The samples hydrated for 20 min and were further investigated via thermal gravimetric analysis after stopping the hydration. It is concluded that the initial peak originated from the formation of portlandite due to free lime dissolution as shown in Fig. 7 (g, h). That is why the contribution of heat signal due to free lime reaction is removed from the cumulative heat release of all the sample. As a result, the Ref. (−O) sample exhibited the highest cumulative heat release (~56 J/g), while a nominal ~1–7 J/g cumulative heat of hydration was observed in all the Cr and V doped C_2S with varying water to solid ratio. It is known that the presence of lime decreases the dissolution of C_2S, and the Ref. (-O) (2.7 wt%) contains the highest amount of free lime (Tables 3 and 4) (Nicoleau et al., 2013) but it is also the most reactive. Incorporation of minor ions such as K or B into C_2S is reported to improve hydration activity due to the stabilization of high-temperature polymorphs (α′ and β-C_2S) (Cuesta et al., 2021; El-Didamony et al., 1996; Parkash et al., 2015b). However, Cr and V-containing samples exhibited minimal reactivity. Even having α′ (5-9 wt%) and β -C_2S (71–88 wt%) in the Cr5-O and V5-O sample as compared to Ref. (-O) β (75 wt%)/γ -C_2S (17 wt%), the early stage (48–72 h) C_2S reactivity is not improved.

As the dissolution of solids is a surface phenomenon, the rate of dissolution is dependent on the total surface area of the dissolving solid as shown in the general rate law expression (1). The specific surface area (SSA) of the sieved sample exhibited that the Ref. (O) (3.8 m^2/g) contains the highest available surface for the reaction (Table 2). Therefore, the lower reactivity of Cr5-O and V5-O samples than the Ref. (-O) can also be attributed to the less available surface for the reaction with water (Brand et al., 2019).

The dissolution rate should follow a general law such as,

$$Rate = k.S_{react}(t).f(\Delta G) \quad (1)$$

S_{react}= reactive surface area (m^2/g)
k = rate constant (s^{-1})
f = unknown priori function for free enthalpy
ΔG = Gibbs free energy change (kJ/mol)

Persuasively, the early age (48–72 h) of C_2S reactivity is more dependent on the available SSA than lime, w/s ratio, and the type of C_2S polymorph.

3.3. Leaching behavior

The leaching of Cr and V doped C_2S under varying (oxidizing and reducing) calcination condition depends on the oxidation state of Cr and V, its substitution amounts, pH, type of mineral phase as well as the kinetic equilibrium between varying oxides of chromate and vanadate. Calcium chromate is soluble at> 20 g/L in the water while calcium vanadate is insoluble at room temperature. The synthesized samples contain C_2S ($K_{sp} = 9.17 \times 10^{-6}$), and free lime (CaO) ($K_{sp} = 4.3 \times 10^{-6}$) that upon hydration can increase the pH of the leachate as shown in the following Eqs. 2,3 (Brand et al., 2019).

$$CaO + H_2O \rightarrow Ca(OH)_{2(aq)} \leftrightharpoons Ca^{2+} + 2OH^- \quad \text{pH} = \quad 12.46 \quad (2)$$

$$Ca_2SiO_4 + 2H_2O \rightarrow 2Ca^{2+} + H_2SiO_4^{2-} + 2OH^- \text{pH} = \quad 10 - 12.5 \quad (3)$$

$$Ca^{2+} + CrO_4^{2-} \leftrightharpoons CaCrO_4 \text{ pH} > 12.0 \quad (4)$$

$$3Ca^{2+} + 2VO_4^{3-} \leftrightharpoons Ca_3(VO_2)_4 \text{pH} > \quad 12.0 \quad (5)$$

The pH of the Cr5-O, Cr10-O, and Cr15-O samples after placing in water for 24 h at a liquid/solid ratio of 10 was found to be in the range of 12.5–13.0. The Cr5-O sample exhibited the highest percentage of Cr, Si, and Ca leaching compared to Cr10-O and Cr15-O samples as shown in Fig. 8(a). The Cr leaching is directly proportional to Si leaching in all the samples synthesized under oxidizing conditions. Moreover, possible aqueous Ca^{2+} concentration is slightly variating in Cr10-O and Cr15-O samples. At pH> 12.0, the dominant species of chromate ion is CrO_4^{2-}. The solubility product (K_{sp}) value of $CaCrO_4$ is 5.1×10^{-6}, and the chemical reaction between Ca^{2+} and CrO_4^{2-} has been shown in Eq. (4). Part of Cr (VI) can be immobilized by the formation of the low solubility chromium complex. But it can be understood with the help of Cr distribution in mineral phases and amorphous content in Cr5-O, Cr10-O, and Cr15-O samples. In Cr5-O, the Cr (VI) can substitute on Si-site in C_2S as shown in Section 3.1.1. The high Cr leaching from the Cr5-O sample is due to the high dissolution of C_2S phases as the high Si leaching supports the idea. As the replacement of Cr increases in Cr10-O and Cr15-O, the more individual grains are covered with a glass layer which restricts the dissolution of C_2S (Fig. 5(a), (b), and (c)) (see Table S7 for QXRD of leachate residues).

The Ca and Cr leaching in the samples produced under reducing conditions decreased as compared to the values calcined under oxidizing conditions as shown in Fig. 8(b). The Cr2R exhibited the highest Cr leaching value while other Cr (4−15) R samples showed a clear decrease in the Cr leaching. This can be attributed to stabilize more Cr as (II and III) upon incremental addition of Cr to the samples (Table 3), which does not occupy the Si-site in C_2S. Therefore, the Cr leaching is directly proportional to the degree of C_2S dissolution.

It is shown in Section 3.1.2 that the V(V) tends to substitute on Si-site in C_2S under oxidizing conditions (V5-O, V10-O, V15-O). Upon dissolution, the type of calcium vanadate precipitates depends on the pH of the leachate. The $Ca(VO_3)_2$ forms around pH 5–8 while $Ca_2V_2O_7$, as well as $Ca_3(VO_4)_2$, are the dominant precipitates at pH 9–10.6 and 10.6–13 respectively (Hobson et al., 2017). The pH of the V5-O, V10-O, and V15-O samples was found in the range of 12.6–12.7. So, the dominant calcium vanadate would be $Ca_3(VO_4)_2$ ($\log K_{sp} = -17.97$) as shown in Eq. 4. The percentage leaching of Si and V from V5-O, V10-O, and V15-O is shown in Fig. 8(c). It can be observed that the maximum V concentration in the leachate is inversely proportional to the aqueous Ca^{2+} concentration. Even the amount of V mol. % is incrementally increasing in the starting sample. But it seems that the percentage concentration of

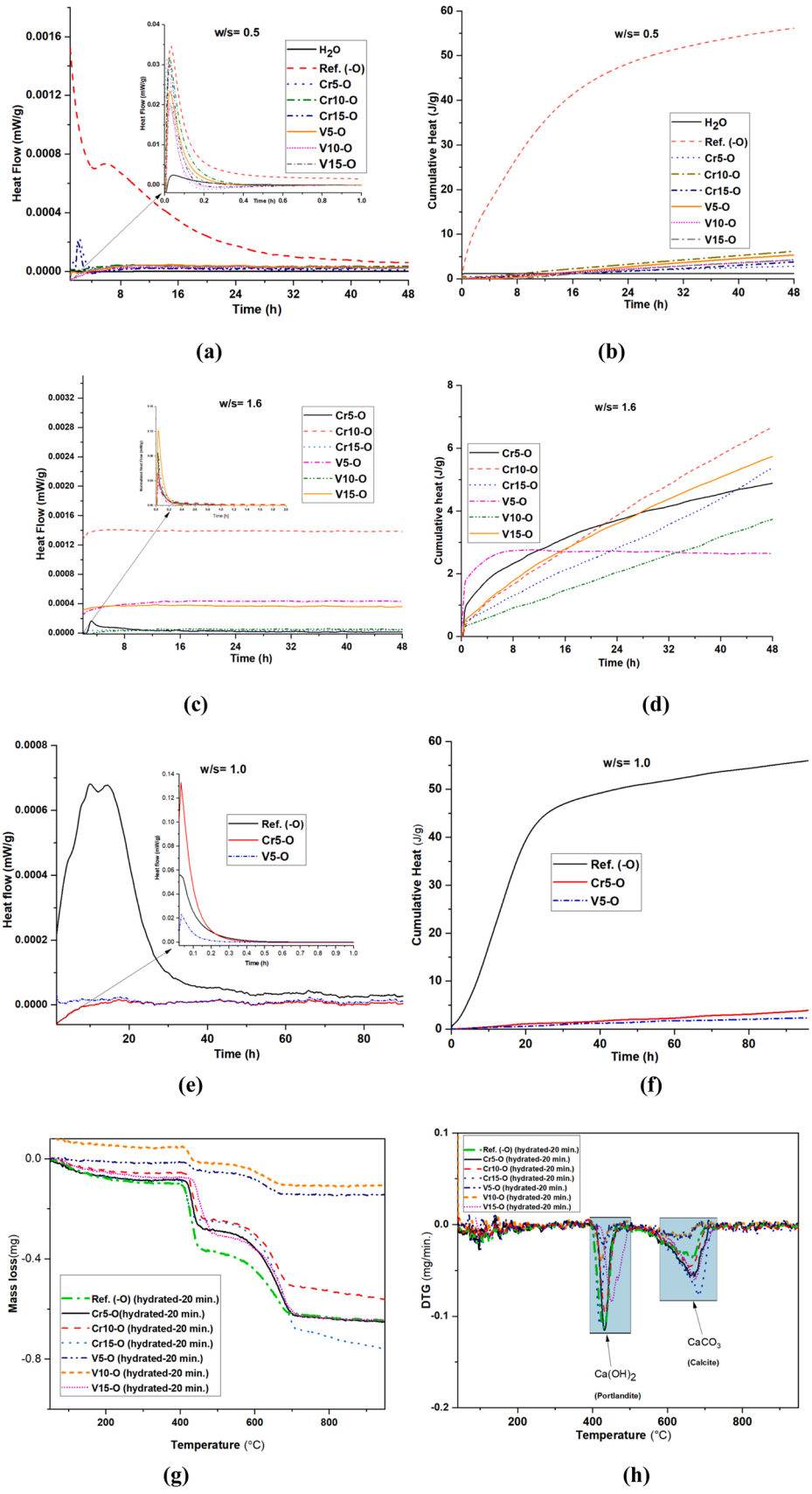

Fig. 7. Heat release of the chromium and vanadium doped C_2S under oxidizing conditions sieved between 20 and 40 μm. with water to solid ratio (a) 0.5 (c) 1.0 (e) 1.6. Cumulative heat release in J/g of the (b) 0.5 (d) 1.0 (e) 1.6. TG curve of the synthesized C_2S samples showing the mass loss in function of temperature (e) mass loss of Cr and V doped C_2S samples under oxidizing conditions in first 20 min of hydration (f) DTG curve of the synthesized C_2S samples showing the mass loss per minute in function of temperature.

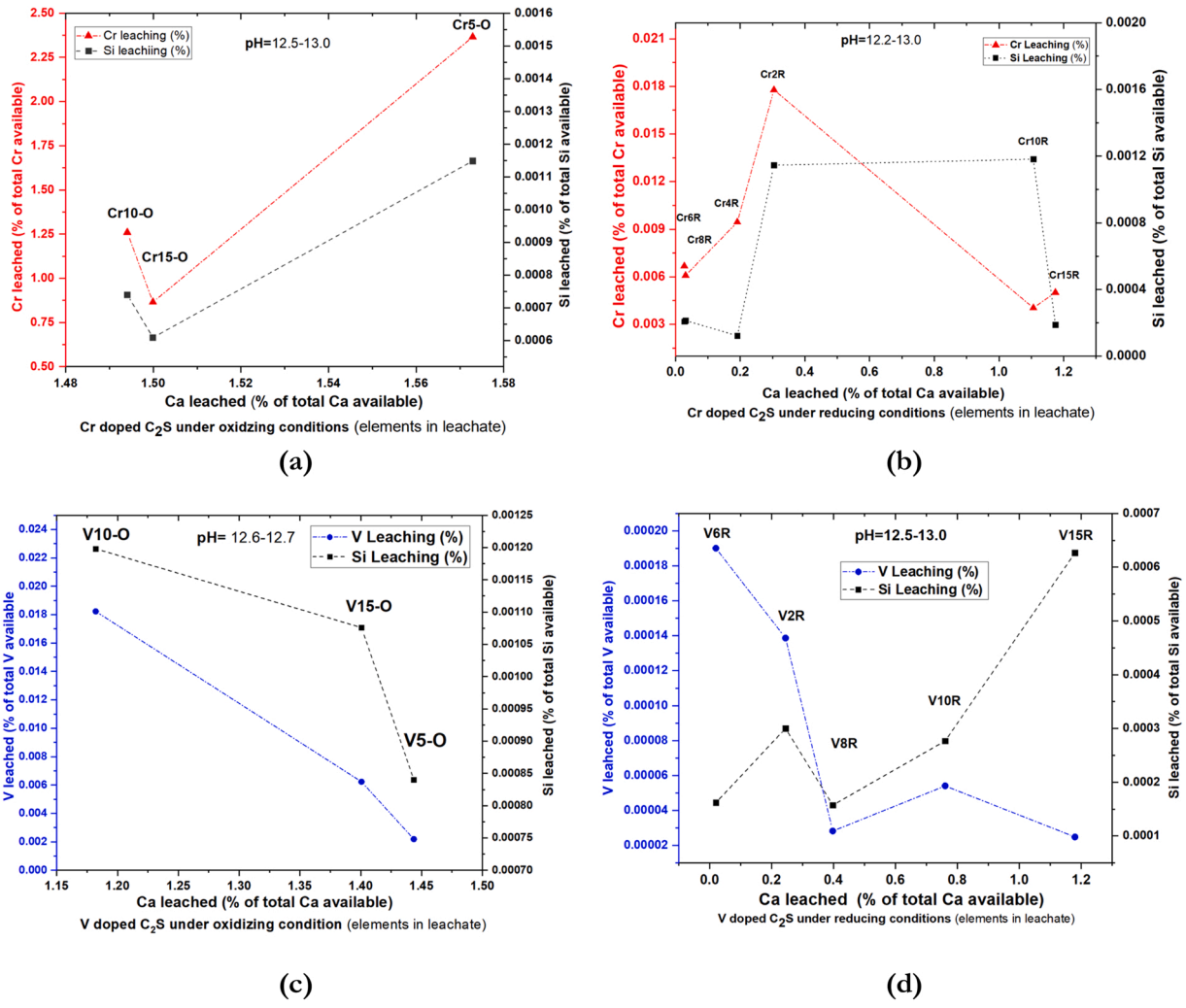

Fig. 8. One batch leaching analysis (w/s = 10) of Cr and V doped C_2S, the amount Si, Cr and V has been plotted as a function of Ca (%) leaching and pH range mentioned on the graph (a) Cr doped C_2S under oxidizing conditions (b) Cr doped C_2S under reducing conditions (c) V doped under oxidizing conditions (d) V doped under reducing conditions.

V leaching is controlled by the percentage of aqueous Ca^{2+} presence in the leachate. The sample V10-O exhibited the highest percentage of V (0.018 %) leaching but the lowest percentage of Ca^{2+} (1.16 %) leaching while the V15-O contains the highest amount of V in the C_2S matrix phases. This can be understood by considering the source of Ca^{2+} in the leachate. The V10-O sample contains the lowest amount of free lime (0.1 wt%) as one of the active sources of aqueous Ca^{2+}. While the V15-O sample exhibited high free lime (1.6 wt%) and calcite (1.6 wt%). The presence of dissolved CO_2 in solution (leads to the formation of $CaCO_3$ ($K_{sp} = 3.36 \times 10^{-9}$)) provides a sink for calcium in the leachate due to lower solubility of calcium carbonate than calcium hydroxide. Moreover, the aqueous Ca^{2+} concentration developing from C_2S dissolution results in vanadate concentration either at or very close to the solubility limit of $Ca_3(VO_4)_2$ which limits the concentration of vanadate in solution. Conclusively, the amount of V leaching is independent of the starting amount of V in the C_2S matrix. It depends on the active aqueous Ca^{2+} source in the solution, the type of calcium vanadate complex, and pH. The amount of percentage leaching of Si is directly proportional to the amount of V concentration in the leachate which indicated the degree of dissolution of C_2S phases and active occupation of V_2O_5 on the Si-site. The dissolution of C_2S which also leads to the formation of Ca-Si-H can also actively uptake some V_2O_5 on tetrahedral Si-sites (Hobson et al., 2017).

In reducing conditions, overall calcium, silicon, and vanadium leaching decrease as compared to oxidizing condition samples as shown in Fig. 8(b). As we have seen above, the leaching of vanadium is controlled by the active calcium source in the leachate. The vanadium leaching is inversely proportional to calcium concentration in the leachate. The reducing sample contains a high amount of free lime (4.2–9.4 wt%) that would limit the solubility of $Ca_3(VO_4)_2$ like the sample under oxidizing conditions.

4. Summary and Conclusion

The Cr (0–15 mol%) and V (0–15 mol%) incorporation on the Si-site in C_2S was investigated using sol-gel synthesis under oxidizing and reducing (20 %CO/80 % CO_2) conditions. The C_2S polymorphs stability, the effect of varying calcination conditions on heavy metals (Cr, V) incorporation as well as the oxidation state, and microstructure along with early age (48–72 h) hydration at different water to solid ratio and the leaching behavior. The important findings are as follows.

1. The C_2S can incorporate Cr (VI) and V(V) on Si-site in C_2S under air-oxidizing conditions. This led to stabilization of the high-temperature α, β-C_2S polymorphs as shown in Cr5-O and V5-O samples. A Cr and V content higher than 5 mol% started to stabilize heavy metal (Cr and V) bearing amorphous phases due to the substitution limit. The stabilization of α-C_2S in Cr-containing samples

can be attributed to the matrix constraint due to the glass layer covering individual C_2S particles. In addition to that, a twin domain was observed in the V5-O sample which is the characteristic deformation that evolved during the α′→β transition due to doping of foreign ions in C_2S. A constant amount of Cr (VI) can substitute on Si-site in C_2S which is independent of the starting amount of Cr in the sample. The remaining chromium oxide prefers to stay Cr (III) as the most stable oxidation state. A maximum of 4.1 mol% Cr can be substituted on Si-site in C_2S theoretically while it was difficult to predict the maximum substitution of V due to high amorphous content in the sample.

2. Cr and V oxide tend not to replace Si in C_2S under reducing conditions (20 % CO/80 % CO_2) due to oxidation state mismatch. The Cr was present as (II) and (III) oxidation states in Cr2R-Cr15R samples which led to the formation of high CaO and (Para)wollastonite phases due to calcium to silica ratio of less than 2. The V2R-V15R samples also contain calcium vanadate phases with high amorphous content (2.9–24.5 wt%), (Para)wollastonite (6.4–12.4 wt%), and lime (4.2–9.4 wt%) indicating Si deficit for C_2S synthesis. The incorrect stoichiometry stipulated that V and Cr were not available in a favorable oxidation state to be incorporated in C_2S at high temperatures.
3. The incorporation of V and Cr into C_2S stabilizes the reactive α′/β-C_2S but drastically reduces the early-stage hydration activity of C_2S compared to the Ref. (-O) sample. Even though the reference sample contains a significant amount of γ which is non-reactive as well as free lime that also reduces the solubility of C_2S. The specific surface area for the reference is higher than for the doped samples making it reactive at early age hydration.
4. The V (V) and Cr (VI) substituted on Si-site in C_2S exhibited higher mobility than Cr (II) (III) containing C_2S samples. The Cr leaching is sensitive to the oxidation state as well as the Cr-bearing amorphous phases in the sample. Even having the mobile Cr (VI) oxidation state, the coverage of Cr grains with a glass layer decreases the dissolution degree of solid and leaching. Once Cr (VI) is substituted on Si-site in C_2S, the Cr leaching is directly proportional to the degree of C_2S phase dissolution.
5. The vanadium leaching is controlled by the active source of aqueous Ca^{2+} which is independent of the starting amount of V in the sample. The V leaching is inversely proportional to the aqueous Ca^{2+} in the leachate due to the formation of $Ca_3(VO_4)_2$ at pH > 12. The directly proportional relationship between V and Si leaching in the V5O, V10O, and V15O samples explained that the V_2O_5 was released from the Si site of C_2S. The Si leaching from V2R, V4R, V6R, V8R, V10R, and V15R samples was independent of V leaching indicating the source of V_2O_5 is not the Si-site of C_2S.

CRediT authorship contribution statement

Muhammad Jawad Ahmed: Conceptualization, methodology, validation, investigation, writing – original draft, Writing – review & editing, **Remco Cuijpers**: Conceptualization, methodology, investigation, validation, **Mary Van Wijngaarden-Kroft**: methodology, investigation, **Tiny Verhoeven**: methodology, investigation, **Katrin Schollbach**: Resources, visualization- review & editing, supervision, **Sieger Van Der Laan**: Resources, visualization- review & editing, supervision, **H.J.H. Brouwers**: Resources, visualization- review & editing, project administration, supervision.

Declaration of Competing Interest

The authors declare that they have no known competing financial interests or personal relationships that could have appeared to influence the work reported in this paper.

Data availability

Data will be made available on request.

Acknowledgment

The authors would like to acknowledge the financial support from NWO (The Netherlands Organisation for Scientific Research) for funding this research (project no.10023338) and M2i (Materials Innovation Institute, project no. S81.6.15565b) for managing this project. Furthermore, the authors wish to express their gratitude to the following sponsors of this research: Tata Steel; ENCI; V.d. Bosch Beton; Blue phoenix group; Hess.

Appendix A. Supporting information

Supplementary data associated with this article can be found in the online version at doi:10.1016/j.jhazmat.2022.130032.

References

Adendorff, K.T., de Villiers, J.P.R., Kruger, G.J., 1992. Crystal structures of Ca5Cr3O12 and Ca5Cr2SiO12, the chromium analogs of silicocarnotite. J. Am. Ceram. Soc. 75, 1416–1422. https://doi.org/10.1111/J.1151-2916.1992.TB04203.X.

Alam, Q., Schollbach, K., Rijnders, M., van Hoek, C., van der Laan, S., Brouwers, H.J.H., 2019. The immobilization of potentially toxic elements due to incineration and weathering of bottom ash fines. J. Hazard. Mater. 379, 120798 https://doi.org/10.1016/J.JHAZMAT.2019.120798.

Apte, A.D., Tare, V., Bose, P., 2006. Extent of oxidation of Cr(III) to Cr(VI) under various conditions pertaining to natural environment. J. Hazard. Mater. 128, 164–174. https://doi.org/10.1016/J.JHAZMAT.2005.07.057.

Aranda, M.A.G., 2016. Recent studies of cements and concretes by synchrotron radiation crystallographic and cognate methods. Crystallogr. Rev. 22, 150–196. https://doi.org/10.1080/0889311X.2015.1070260.

Basak, A., Ramrakhiani, L., Ghosh, S., Sen, R., Mandal, A.K., 2018. Preparation of chromium doped phosphate glass adopting microwave irradiation and comparative analysis of properties with conventional glass. J. Non Cryst. Solids 500, 11–17. https://doi.org/10.1016/J.JNONCRYSOL.2018.04.014.

Benhelal, E., Zahedi, G., Shamsaei, E., Bahadori, A., 2013. Global strategies and potentials to curb CO_2 emissions in cement industry. J. Clean. Prod. 51, 142–161. https://doi.org/10.1016/j.jclepro.2012.10.049.

Black, L., Stumm, A., Garbev, K., Stemmermann, P., Hallam, K.R., Allen, G.C., 2003. X-ray photoelectron spectroscopy of the cement clinker phases tricalcium silicate and β-dicalcium silicate. Cem. Concr. Res. 33, 1561–1565. https://doi.org/10.1016/S0008-8846(03)00097-8.

Black, L., Stumm, A., Garbev, K., Stemmermann, P., Hallam, K.R., Allen, G.C., 2003a. X-ray photoelectron spectroscopy of the cement clinker phases tricalcium silicate and β-dicalcium silicate. Cem. Concr. Res. 33, 1561–1565. https://doi.org/10.1016/S0008-8846(03)00097-8.

Black, L., Garbev, K., Stemmermann, P., Hallam, K.R., Allen, G.C., 2003b. Characterisation of crystalline C-S-H phases by X-ray photoelectron spectroscopy. Cem. Concr. Res. 33, 899–911. https://doi.org/10.1016/S0008-8846(02)01089-X.

Brand, A.S., Gorham, J.M., Bullard, J.W., 2019. Dissolution rate spectra of β-dicalcium silicate in water of varying activity. Cem. Concr. Res. 118, 69–83. https://doi.org/10.1016/J.CEMCONRES.2019.02.014.

Chan, C.J., Kriven, W.M., Young, J.F., 1992. Physical stabilization of the β→γ transformation in dicalcium silicate. J. Am. Ceram. Soc. 75, 1621–1627. https://doi.org/10.1111/j.1151-2916.1992.tb04234.x.

Chaurand, P., Rose, J., Briois, V., Olivi, L., Hazemann, J.L., Proux, O., Domas, J., Bottero, J.Y., 2007. Environmental impacts of steel slag reused in road construction: a crystallographic and molecular (XANES) approach. J. Hazard. Mater. https://doi.org/10.1016/j.jhazmat.2006.02.060.

Chen, Y.L., Lai, Y.C., Lin, C.J., Chang, Y.K., Ko, M.S., 2013. Controlling sintering atmosphere to reduce the hazardous characteristics of low-energy cement produced with chromium compounds. J. Clean. Prod. 43, 45–51. https://doi.org/10.1016/J.JCLEPRO.2012.12.027.

Cuesta, A., Ayuela, A., Aranda, M.A.G., 2021. Belite cements and their activation. Cem. Concr. Res. 140, 106319 https://doi.org/10.1016/j.cemconres.2020.106319.

El-Didamony, H., Sharara, A.M., Helmy, I.M., Abd El-Aleem, S., 1996. Hydration characteristics of β-C2S in the presence of some accelerators. Cem. Concr. Res. 26, 1179–1187. https://doi.org/10.1016/0008-8846(96)00103-2.

A. Elhoweris, I. Galan, F.P. Glasser, Stabilisation of α′ dicalcium silicate in calcium sulfoaluminate clinker, Https://Doi.Org/10.1680/Jadcr.18.00050. 32 (2020b) 112–124. ⟨doi:10.1680/JADCR.18.00050⟩.

A. Elhoweris, I. Galan, F.P. Glasser, Stabilisation of α′ dicalcium silicate in calcium sulfoaluminate clinker, Https://Doi.Org/10.1680/Jadcr.18.00050. 32 (2020a) 112–124. ⟨doi:10.1680/JADCR.18.00050⟩.

El-Moneim, A.A., Hashem, H.A., El-Namrouty, A.A., Atef, A., 2022. Effect of V2O5 on structural and elastic properties of alkali silicate SiO2–Na2O–NaF glasses. J. Non Cryst. Solids 580, 121389. https://doi.org/10.1016/J.JNONCRYSOL.2021.121389.

Fierens, P., Tirlocq, J., 1983. Nature and concentration effect of stabilizing elements of beta-dicalcium silicate on its hydration rate. Cem. Concr. Res. 13, 267–276. https://doi.org/10.1016/0008-8846(83)90110-2.

Frederickson, L.D., Hausen, D.M., 2002. Infrared spectra-structure correlation study of vanadium-oxygen compounds. Anal. Chem. 35, 818–827. https://doi.org/10.1021/AC60200A018.

Georgescu, M., Tipan, J., Badanoiu, A., Crisan, D., Dragan, I., 2000. Highly reactive dicalcium silicate synthesized by hydrothermal processing. Cem. Concr. Compos. https://doi.org/10.1016/S0958-9465(00)00017-2.

Ghose, A., Chopra, S., Young, J.F., 1983. Microstructural characterization of doped dicalcium silicate polymorphs. J. Mater. Sci. 18, 2905–2914. https://doi.org/10.1007/BF00700771.

Goh, C.L., Gan, S.L., 1996. Change in cement manufacturing process, a cause for decline in chromate allergy? Contact Dermat. 34, 51–54. https://doi.org/10.1111/J.1600-0536.1996.TB02112.X.

Guo, P., Wang, B., Bauchy, M., Sant, G., 2016. Misfit stresses caused by atomic size mismatch: the origin of doping-induced destabilization of dicalcium silicate. Cryst. Growth Des. https://doi.org/10.1021/acs.cgd.5b01740.

Hobson, A.J., Stewart, D.I., Bray, A.W., Mortimer, R.J.G., Mayes, W.M., Rogerson, M., Burke, I.T., 2017. Mechanism of vanadium leaching during surface weathering of basic oxygen furnace steel slag blocks: a microfocus X-ray absorption spectroscopy and electron microscopy study. Environ. Sci. Technol. 51, 7823–7830. https://doi.org/10.1021/ACS.EST.7B00874/SUPPL_FILE/ES7B00874_SI_001.PDF.

Jawad Ahmed, M., Schollbach, K., van der Laan, S., Florea, M., Brouwers, H.J., 2022. A quantitative analysis of dicalcium silicate synthesized via different sol-gel methods. Mater. Des. 213, 110329 https://doi.org/10.1016/j.matdes.2021.110329.

Kaja, A.M., Delsing, A., van der Laan, S.R., Brouwers, H.J.H., Yu, Q., 2021. Effects of carbonation on the retention of heavy metals in chemically activated BOF slag pastes. Cem. Concr. Res. 148, 106534 https://doi.org/10.1016/J.CEMCONRES.2021.106534.

Kumar, A., Rahman, F., Khan, A., 2021. Fabrication and characterization of VO2 nanoparticles: a simple and low-cost combustion method. AIP Conf. Proc. 2369, 020019 https://doi.org/10.1063/5.0060865.

Lai, G.C., Nojiri, T., Ichi Nakano, K., 1992. Studies of the stability of β-Ca2SiO4 doped by minor ions. Cem. Concr. Res. 22, 743–754. https://doi.org/10.1016/0008-8846(92)90097-F.

Li, J., Geng, G., Zhang, W., Yu, Y.S., Shapiro, D.A., Monteiro, P.J.M., 2019. The hydration of β- And α′ H -dicalcium silicates: an X-ray spectromicroscopic study. ACS Sustain. Chem. Eng. 7, 2316–2326. https://doi.org/10.1021/acssuschemeng.8b05060.

Li, X., He, C., Bai, Y., Ma, B., Wang, G., Tan, H., 2014. Stabilization/solidification on chromium (III) wastes by C3A and C3A hydrated matrix. J. Hazard. Mater. 268, 61–67. https://doi.org/10.1016/J.JHAZMAT.2014.01.002.

Lin, C.K., Chen, J.N., Lin, C.C., 1996. An NMR and XRD study of solidification/stabilization of chromium with Portland cement and β-C2S. J. Hazard. Mater. 48, 137–147. https://doi.org/10.1016/0304-3894(95)00154-9.

Lopatin, D.V., Chizhikova, V.M., 2007. Crystal-chemical stabilization of dicalcium silicate. Steel Transl. 373, 191–195. https://doi.org/10.3103/S0967091207030035.

Lu, M., Li, Q., Zhou, C., Zhang, G.P., Bai, Y.H., Zimmermann, R., Claessen, R., Reinert, F., Steiner, P., Hüfner, S., 1998. Strong hybridization in vanadium oxides: evidence from photoemission and absorption spectroscopy. J. Phys. Condens. Matter 10, 5697. https://doi.org/10.1088/0953-8984/10/25/018.

Ludwig, H.M., Zhang, W., 2015. Research review of cement clinker chemistry. Cem. Concr. Res. https://doi.org/10.1016/j.cemconres.2015.05.018.

Maycock, J.N., McCarty, M., 1973. Crystal lattice defects in di-calcium silicate. Cem. Concr. Res. 3, 701–713. https://doi.org/10.1016/0008-8846(73)90005-7.

Meiszterics, A., Rosta, L., Peterlik, H., Rohonczy, J., Kubuki, S., Henits, P., Sinkó, K., 2010. Structural characterization of gel-derived calcium silicate systems. J. Phys. Chem. A. 114, 10403–10411. https://doi.org/10.1021/jp1053502.

Miyata, H., Fujii, K., Ono, T., Kubokawa, Y., Ohno, T., Hatayama, F., 1987. Fourier-transform infrared investigation of structures of vanadium oxide on various supports. J. Chem. Soc. Faraday Trans. 1 Phys. Chem. Condens. Phases 83, 675–685. https://doi.org/10.1039/F19878300675.

Neuhold, S., van Zomeren, A., Dijkstra, J.J., van der Sloot, H.A., Drissen, P., Algermissen, D., Mudersbach, D., Schüler, S., Griessacher, T., Raith, J.G., Pomberger, R., Vollprecht, D., 2019. Investigation of possible leaching control mechanisms for chromium and vanadium in electric arc furnace (EAF) slags using combined experimental and modeling approaches. Minerals. https://doi.org/10.3390/min9090525.

Nicoleau, L., Nonat, A., Perrey, D., 2013. The di- and tricalcium silicate dissolutions. Cem. Concr. Res. https://doi.org/10.1016/j.cemconres.2013.01.017.

Omotoso, O.E., Ivey, D.G., Mikula, R., 1995. Characterization of chromium doped tricalcium silicate using SEM/EDS, XRD and FTIR. J. Hazard. Mater. 42, 87–102. https://doi.org/10.1016/0304-3894(95)00012-J.

Pang, F., Wei, C., Zhang, Z., Wang, W., Wang, Z., 2022. The migration and immobilization for heavy metal chromium ions in the hydration products of calcium sulfoaluminate cement and their leaching behavior. J. Clean. Prod., 132778 https://doi.org/10.1016/J.JCLEPRO.2022.132778.

R. Parkash, S.K. Mehta, S. Dixit, S. Singh, S.C. Ahluwalia, J.M. Sharma, Effect of chromium addition on the kinetics of hydration of dicalcium silicate phase, Http://Dx.Doi.Org/10.1680/Adcr.2010.22.2.81. 22 (2015a) 81–89. ⟨doi:10.1680/ADCR.2010.22.2.81⟩.

R. Parkash, S.K. Mehta, S. Dixit, S. Singh, S.C. Ahluwalia, J.M. Sharma, Effect of chromium addition on the kinetics of hydration of dicalcium silicate phase, Http://Dx.Doi.Org/10.1680/Adcr.2010.22.2.81. 22 (2015b) 81–89. ⟨doi:10.1680/ADCR.2010.22.2.81⟩.

Pérez-Villarejo, L., Martínez-Martínez, S., Carrasco-Hurtado, B., Eliche-Quesada, D., Ureña-Nieto, C., Sánchez-Soto, P.J., 2015. Valorization and inertization of galvanic sludge waste in clay bricks. Appl. Clay Sci. 105–106, 89–99. https://doi.org/10.1016/J.CLAY.2014.12.022.

Romano, J.S., Rodrigues, F.A., 2008. Cements obtained from rice hull: Encapsulation of heavy metals. J. Hazard. Mater. 154, 1075–1080. https://doi.org/10.1016/J.JHAZMAT.2007.11.051.

Saidani, S., Smith, A., El Hafiane, Y., Ben Tahar, L., 2018. Re-examination of the β→γ transformation of Ca2SiO4. J. Eur. Ceram. Soc. 38, 4756–4767. https://doi.org/10.1016/j.jeurceramsoc.2018.06.011.

Saidani, S., Smith, A., El Hafiane, Y., Ben Tahar, L., 2021. Role of dopants (B, P and S) on the stabilization of β-Ca2SiO4. J. Eur. Ceram. Soc. 41, 880–891. https://doi.org/10.1016/J.JEURCERAMSOC.2020.07.037.

Silva, M.A.R., Mater, L., Souza-Sierra, M.M., Corrêa, A.X.R., Sperb, R., Radetski, C.M., 2007. Small hazardous waste generators in developing countries: use of stabilization/solidification process as an economic tool for metal wastewater treatment and appropriate sludge disposal. J. Hazard. Mater. 147, 986–990. https://doi.org/10.1016/J.JHAZMAT.2007.01.128.

Silversmit, G., Depla, D., Poelman, H., Marin, G.B., De Gryse, R., 2004. Determination of the V2p XPS binding energies for different vanadium oxidation states (V5+ to V0+). J. Electron Spectrosc. Relat. Phenom. 135, 167–175. https://doi.org/10.1016/J.ELSPEC.2004.03.004.

Spooren, J., Kim, E., Horckmans, L., Broos, K., Nielsen, P., Quaghebeur, M., 2016. In-situ chromium and vanadium recovery of landfilled ferrochromium and stainless steel slags. Chem. Eng. J. 303, 359–368. https://doi.org/10.1016/J.CEJ.2016.05.128.

Stewart, D.I., Bray, A.W., Udoma, G., Hobson, A.J., Mayes, W.M., Rogerson, M., Burke, I.T., 2018. Hydration of dicalcium silicate and diffusion through neo-formed calcium-silicate-hydrates at weathered surfaces control the long-term leaching behaviour of basic oxygen furnace (BOF) steelmaking slag. Environ. Sci. Pollut. Res. 25, 9861–9872. https://doi.org/10.1007/S11356-018-1260-7/FIGURES/5.

Suzuki, M., Umesaki, N., Okajima, T., Tanaka, T., 2016. Formation and local structure analysis of high-valence chromium ion in dicalcium silicate. J. Am. Ceram. Soc. 99, 3151–3158. https://doi.org/10.1111/JACE.14337.

Thomas, J.J., Ghazizadeh, S., Masoero, E., 2017. Kinetic mechanisms and activation energies for hydration of standard and highly reactive forms of β-dicalcium silicate (C2S). Cem. Concr. Res. 100, 322–328. https://doi.org/10.1016/j.cemconres.2017.06.001.

Trezza, M.A., Scian, A.N., 2007. Waste with chrome in the Portland cement clinker production. J. Hazard. Mater. 147, 188–196. https://doi.org/10.1016/J.JHAZMAT.2006.12.082.

van Zomeren, A., van der Laan, S.R., Kobesen, H.B.A., Huijgen, W.J.J., Comans, R.N.J., 2011. Changes in mineralogical and leaching properties of converter steel slag resulting from accelerated carbonation at low CO 2 pressure. Waste Manag. 31, 2236–2244. https://doi.org/10.1016/j.wasman.2011.05.022.

Z. Wensheng, R. Xuehong, O. Shixi, 硅 酸 盐 学 报 Development on Ion Substitution Effect on the Crystal Structure and Properties of Tricalcium Silicate, (n.d.). ⟨http://www.cnki.net/kcms/detail/11.2310.TQ.20110927.1349.024.html⟩ (accessed September 7, 2022).

Wesselsky, A., Jensen, O.M., 2009. Synthesis of pure Portland cement phases. Cem. Concr. Res. https://doi.org/10.1007/s11368-012-0598-6.

Wu, L., Zhou, Y., Dong, Y., 2013. Precipitation behavior of V-enrichment mineral in steelmaking slag bearing vanadium modified by SiO2. Appl. Mech. Mater. 295–298, 1729–1734. https://doi.org/10.4028/WWW.SCIENTIFIC.NET/AMM.295-298.1729.

Wu, X., Li, L., Dong, Y., 2011. Enrichment and crystallization of vanadium in factory steel slag. Metallurgist 55, 401–409. https://doi.org/10.1007/S11015-011-9444-0/FIGURES/7.

Zhu, J., Yang, K., Chen, Y., Fan, G., Zhang, L., Guo, B., Guan, X., Zhao, R., 2021. Revealing the substitution preference of zinc in ordinary Portland cement clinker phases: A study from experiments and DFT calculations. J. Hazard. Mater. 409, 124504 https://doi.org/10.1016/J.JHAZMAT.2020.124504.